

THE UNIVERSITY OF CHICAGO

BIG ASS WASTE OF TIME

A DISSERTATION SUBMITTED TO
THE FACULTY OF THE DIVISION OF THE PHYSICAL & BIOLOGICAL
SCIENCES

IN CANDIDACY FOR THE DEGREE OF
DOCTOR OF PHILOSOPHY

DEPARTMENT OF BIOPHYSICAL SCIENCE

BY
WILL MCFADDEN

CHICAGO, ILLINOIS

SEPT 2016

To

ABSTRACT

Blar Blar

ACKNOWLEDGEMENTS

I'd like to thank Patrick McCall, Pete Dahlberg, and Claire Stevenson for being there for me.

TABLE OF CONTENTS

ABSTRACT	iii
ACKNOWLEDGEMENTS	iv
1 INTRODUCTION	1
1.1 Introduction	2
1.1.1 Short Timescale Mechanics of Cross-linked Actin Filament Networks	2
1.1.2 Long Timescale Stress Relaxation from Transient Cross-link Unbinding	4
1.2 Introduction	5
2 IMPACT OF FILAMENT RECYCLING ON CORTICAL FLOW IN ANIMAL CELLS	9
3 MODELING 2D ACTIVE NETWORKS WITH RECYCLING	10
3.1 Models	10
3.1.1 Asymmetric filament compliance	10
3.1.2 Drag-like coupling between overlapping filaments	11
3.1.3 Active coupling for motor driven filament interactions	12
3.1.4 2D network formation	13
3.1.5 External applied stress	13
3.1.6 Modeling filament turnover	14
3.1.7 Simulation methods	15
4 FILAMENT RECYCLING AND SUSTAINED CONTRACTILE FLOWS IN AN ACTOMYOSIN NETWORK	18
4.1 Results and Discussion	18
4.1.1 Filament recycling prevents cortical tearing and modulates the viscous stress relaxation of passive filament networks	18
4.1.2 Filament recycling allows persistent stress buildup in active networks	26
4.1.3 Filament recycling tunes the balance between active stress buildup and viscous stress relaxation to generate flows	32
4.2 Conclusion	36
4.3 Supporting Information	37

5	A MODEL OF UPSTREAM ACTOMYOSIN REGULATORS IN PULSED CONTRACTIONS	42
6	PHASES OF DEFORMATION IN FILAMENT NETWORKS WITH CROSS-LINK SLIP	43
6.1	Results	43
6.1.1	Steady-state Approximation of Effective Viscosity	43
6.1.2	Effects of Filament Compliance	46
6.1.3	Alignment at High Strain and Network Tearing	49
6.1.4	Phase Diagram of Dominant Behavior	49
6.1.5	Frequency dependent modulus	51
6.1.6	Strain Memory	52
6.2	Summary and Conclusions	55
6.3	Network Tearing under Extensional Stress	56
6.3.1	Extensional Thinning and Network Tearing	56
6.3.2	Tearing Events During Extensional Strain	56
6.4	Deriving Molecular Drag Coefficients	56
7	DISCUSSION AND FUTURE DIRECTIONS	59
A	WORKSHOP ON MODELING IN BIOLOGY	60
B	ARTISTIC INTERPRETATIONS OF FILAMENT RECYCLING	61
C	REDUCING POWER CONSUMPTION IN HIGH PERFORMANCE COMPUTING	62
C.1	Introduction	62
C.1.1	Alternative Demand Response Options in Data Centers	63
C.2	Problem Statement	65
C.2.1	Modeling Energy Costs	65
C.2.2	Response to a Temporary Price Spike	66
C.3	EDEALS: Electricity Demand-response Easy Adjusted Load Shifting	68
C.4	Small-Scale Evaluation of EDEALS	70
C.4.1	Experimental Setup	70
C.4.2	Evaluation of Model Parameters	70
C.4.3	Relative Energy Savings and Max Wait Times	71
C.5	Conclusion: Implication for An Operational HPC Datacenter	72
C.6	Acknowledgments	73
C.7	Availability	74

LIST OF FIGURES

3.1	<p>Schematic of modeling framework. a) Asymmetric filament compliance. Filaments have smaller spring constant for compression than for extension. b) Cross-link slip. Cross-links are coupled by an effective drag, such that their relative motion is proportional to any applied force. c) Motor activity. Filament activity manifests as a basal sliding rate even in the absence of an external force. Fractional activity. Only a subset of filament cross-links are active, resulting in differential force exertion along the filament. d) Filament recycling. Filaments are turned over at a constant rate, leading to a refreshing in the strain state of all filaments after a characteristic timescale. e) Applied stress. In simulations with passive cross-links, and external stress is applied as force field acting on a fixed spatial domain.</p>	17
4.1	<p>Networks with passive cross-links and no filament turnover undergo three stages of deformation in response to an extensional force. a) Three successive time points from a simulation of a $4 \times 6.6 \mu m$ network deforming under an applied extensional stress of $0.005 \text{ nN}/\mu m$ (stress is applied to filaments in the region indicated by the tan bar). Network deforms to a final dimension of $\sim 4 \times 10 \mu m$. In this and all subsequent figures, filaments are color-coded with respect state of strain (blue = tension, red = compression). Network parameters: $L = 1 \mu m$, $l_c = 0.3 \mu m$, $\xi = 100 \text{ nN} \cdot s/\mu m$. b) Mean filament stress and velocity profiles for the network in (a) at $t=88s$. Note that the stress is nearly constant and the velocity is nearly linear as predicted for a viscous fluid under extension. c) Plots of the mean stress and strain vs time for the simulation in (a), illustrating the three stages of deformation: (i) A fast initial phase accompanies rapid buildup of internal network stress; (ii) after a characteristic time τ_c (indicated by vertical dotted line) the network deforms like a material with a constant effective viscosity, η_c, as indicated by the slope of the dashed line; (iii) at long times, the strain accelerates (see inset) as the network undergoes strain thinning and eventually tears.</p>	20

4.2	Network architecture sets the rate and timescales of deformation. a) The effective viscosity depends on the drag coefficient and the density of the network. Data points are the normalized effective viscosity from simulations (effective viscosity measured in fluid phase divided by the cross link friction coefficient) vs the number of cross links per filament ($L/l_c - 1$). Dotted line indicates the relationship predicted by a simple theory, $\eta_c = \xi(L/l_c - 1)^2$ b) The transition to viscous behavior occurs at a characteristic time, τ_c	22
4.3	Filament recycling modulates effective viscosity in two regimes. a) Examples of $20 \times 12 \mu m$ network under $0.001 \text{ nN}/\mu m$ extensional stress with recycling ($\tau_r = 10s$) and without, ($\tau_r = \infty$). Both images are taken when the patches had reached a net strain of 0.4. The network with recycling doesn't appear to change shape because its components have been recycled to remain in the original domain. Network parameters: $L = 3 \mu m$, $l_c = 0.5 \mu m$, $\xi = 10 \text{ nN} \cdot s/\mu m$. b) Strain curves for identical networks with varying levels of filament recycling. Network parameters: $L = 3 \mu m$, $l_c = 0.5 \mu m$, $\xi = 10 \text{ nN} \cdot s/\mu m$. c) Plotting the effective viscosity derived from the slopes of the lines in panel a. d) Effective viscosities (normalized by the effective viscosity in the absence of recycling, η_c) as a function of the normalized recycling time. When the recycling timescale is significantly less than the passive relaxation timescale, the viscosity of the network becomes dependent on recycling time. Red dashed line indicates the approximation given in equation 4.3 for $m = 3/4$	23
4.4	In the absence of filament recycling, active networks with free boundaries contract and then stall against passive resistance to network compression. a) Example of an active network contracting. Note the buildup of compressive stress as contraction approaches stall between 100 s and 150 s. Network parameters: $L = 5 \mu m$, $l_c = 0.3 \mu m$, $\xi = 100 \text{ nN} \cdot s/\mu m$, $v = 0.1 \text{ nN}$. b) Plots showing time evolution of total network strain and the average extensional (blue) or compressive (red) strain on individual filaments. c) The network's ability to deform relies on the magnitude of asymmetric filament compliance. Total network strain also increases with the applied myosin force v . Note that the extent of contraction approaches an asymptotic limit as the stiffness asymmetry approaches a ratio of ~ 100	26

- 4.5 In the absence of filament recycling, active networks can only exert a transient force against a fixed boundary. **a)** Simulation of an active network with fixed boundaries illustrating progressive buildup of internal stress through local filament rearrangement and deformation. Note the progressive buildup of compressive stress on individual filaments. Network parameters: $L = 5 \mu m$, $l_c = 0.3 \mu m$, $\xi = 100 nN \cdot s/\mu m$, $v = 0.1 nN$. **b)** Plots of total network stress and the average extensional (blue) and compressive (red) stress on individual filaments for the simulation shown in (a). Rapid buildup of extensional stress allows the network transiently to exert force on its boundary, but this force is dissipated at longer times as internal extensional and compressive stresses become balanced. **c.** Measurement and prediction of the characteristic time (τ_a) at which the maximum stress is achieved. 28
- 4.6 Filament recycling allows network to exert sustained stress on a fixed boundary. **a)** Snapshots from simulations of active networks with fixed boundaries for different timescales of filament recycling. Network parameters are the same as in Figure 6. Note that significant remodeling occurs for longer recycling times. **b)** Plots of net stress exerted by the network on its boundaries for different recycling times; for long-lived filaments, stress is built rapidly, but then dissipates. Increasing filament turnover rates reduces stress dissipation by recycling compressed filaments; however, very short recycling times prevent any stress from being built up in the first place. **c)** Plotting the steady state stress derived from the long term stress values of the stress in panel b. **d)** Normalized steady state stress as a function of normalized recycling time. The steady state stress is set by the timescale at which the network strain is refreshed relative to the timescale at which the max stress is reached. The values have been normalized to the predicted peak stress, σ_a in the absence of recycling. Blue dashed line indicates the approximation given in equation 4.4 for $n = 1$ 30

4.7	Filament recycling allows sustained flows in networks with non-isotropic activity. a) Example simulations of non-isotropic networks with long ($\tau_r = 1000$) and short ($\tau_r = 33$) recycling timescales. In these networks the left half of the network is passive while the right half is active. Network parameters are same as in Figures 4.5 and 4.6. Importantly, in all simulations $\tau_a < \tau_c$. b) Graph of strain for identical networks with varying recycling timescales. With long recycling times, the network stalls; reducing the recycling timescale allows the network to persist in its deformation. However, for the shortest recycling timescales, the steady state strain begins to slowly return to 0 net motion. c) Graph of network long-term strain rate as a function of recycling timescale for simulations in a) and b). d) Graph of network long-term strain rate as a function of recycling timescale across a wide range of parameter space. Note that networks only begin to maintain long-term flows when the recycling time is less than $100\tau_a$	33
4.8	Filament recycling tunes the magnitudes of both effective viscosity and steady state stress. a) Dependence of steady state stress and effective viscosity on recycling time τ_r under the condition $\tau_c < \tau_a$. b) Same as a), but for the case where $\tau_a < \tau_c$. c,d) Resulting strain rates for network as a function of recycling time τ_r for the regimes in panels a and b.. . . .	34
4.9	Filament recycling influences architectural control of flow rate. a) For a fixed filament recycling time, filament length tuned network deformation rate. b) Recycling rate is independent of cross-link spacing in this parameter space.	36
4.10	Mechanical properties of passive networks. a) Elastic modulus of networks. Our measurements closely match prediction of $G_0 \sim \mu/l_c$. b) Placeholder for inevitably another figure relevant to passive properties.	38
4.11	Mechanical properties of active networks. a) Timescale of maximum strain in networks free to contract. This relationship was found phenomenologically. b) Dependence of network stress on the fraction of cross-links which are active. Note that the network stress approaches 0 as ϕ approaches 0 or 1.	39
4.12	Tearing of active networks is prevented via recycling. a) An active network undergoing large scale deformations due to active filament rearrangements. b) The same network as in a) but with a shorter filament recycling time. c) Time trace of internal stresses for network in panel a. d) Time trace of internal stresses for network in panel b.	40

4.13	Stress and strain profiles of networks with contractile and passive domains. a) Blue line indicates strain velocity profile while orange represents net stress as measured in the main text. b) Same as panel a except for the condition where recycling time is 10 s. Note the increase in net stress and the corresponding increase in flow rate.	41
6.1	Ratio of effective viscosity measured by shear simulation to predicted effective viscosity as a function of connectivity, L/l_c . Inset: Same measurement for extensional simulations	45
6.2	Network and filament strain for different filament drag coefficient parameters. (top) Plot of total strain normalized by the final mean filament strain, $\delta L/L$. Dashed lines show the amount of strain from affine mechanical stretching. (bottom) Standard deviation of filament extension for the networks in A. Note that the creep compliance in A becomes constant (slope 1) only after the spread in filament extension in B stops increasing. Colors indicate unique experimental conditions.	47
6.3	Sublinear network strain ends as change in filament strain decays. (top) Change in standard deviation of filament strain, σ , as a function of strain relative to pure mechanical strain. (bottom) Dependence of strain rate exponent as a function of strain relative to pure mechanical strain, γ_0 . Colors indicate unique experimental conditions.	48
6.4	Creep response of a network transitioning to phase D. (top) Strain curves for a network undergoing large scale deformation. Inset shows strain exponent as a function of strain (exponent passes 1). (bottom) Traces for the variance in filament orientation and number of cross links. Vertical dashed line shows the point where the strain exponent becomes greater than one.	50
6.5	Schematic of the general creep response of compliant filament networks illustrating the 4 phases of deformation: A) rapid mechanical response, B) combination of slow filament stretching and cross-link slip, C) cross-link slip dominated (line indicates slope of one), D) network tearing from filament alignment. Note that the portion of the curve in section D is only a hypothetical continuation of the actual data.	51
6.6	phase diagram of creep response for different filament extension, μ and cross-link friction, ξ . Yellow, green, and purple dots correspond to creep measurements $\gamma \sim t^\alpha$ with $\alpha < 0.92$, $0.92 < \alpha < 0.98$, or $\alpha > 0.98$ respectively. Blue dots represent creep measurements where $\gamma_{total} < 2\gamma_{mechanical}$	52
6.7	Frequency dependent moduli for networks.	53

6.8	Creep curves in the presence of reversing applied stress for (a) nonlinear extension or (b) linear extension. Note that for linear filaments the induced strain returns to approximately 0 after a complete cycle, while in the nonlinear case the cycle is not completely reversible.	54
C.1	Average core usage for a 244 node shared HPC partition in the Midway cluster. Insert shows usage statistics histogram.	63
C.2	Energy monitoring framework.	65
C.3	Diagram of job scheduling during a four node temporary shutdown experiment. Each colored rectangle displays the execution time of a single LAMPPS test job running for approximately 5 minutes.	66
C.4	Total power consumed during experiments where variable numbers of machines were shut down during simulated peak pricing.	67
C.5	Energy usage of test cluster during partial shutdown experiments. Solid lines indicate power usage during the shutdown, while dashed lines indicate power usage after returning to full operation.	68
C.6	Maximum (solid) and mean (dashed) job wait times during partial shutdown experiments.	69
C.7	Power data for test cluster (top) and production cluster (bottom) nodes in presence of variable usage. The slope and intercept of the line are used to determine u_v and u_0 respectively.	71
C.8	Comparison between node level IPMI measurements and rack level CDU measurements. Best fit shows the model relationship used to convert IPMI data to estimated total power draw.	72
C.9	Estimated savings from partial cluster shutdowns.	73

LIST OF TABLES

3.1	Simulation Parameter Values	16
4.1	Simulation Parameter Values	38
C.1	Model parameters estimated for medium scale HPC datacenter. . . .	73

CHAPTER 1

INTRODUCTION

1.1 Introduction

Cross-linked networks of semi-flexible polymers are a class of materials with poorly understood but highly interesting properties. Early studies of semi-flexible polymer networks reconstituted *in vitro* revealed novel, nonlinear rheology, spurring interest from materials scientists[?]. Cross-linked networks of cytoskeletal polymers have been a subject of great interest to biologists because of their importance as structural components of cells[?, ?].

On shorter timescales, the response of cross-linked polymer networks to applied stress can be well-described theoretically in terms of purely elastic mechanical resistance. On longer timescales, the network’s elastic resistance begins to give way to a viscous relaxation of stored stress, but the mechanisms that govern this viscous relaxation remain poorly understood. It is important to understand the mechanism behind this long timescale relaxation of cross-linked polymer networks both for understanding their novel material properties as well as understanding how this effect may govern physiologically important cellular processes[?].

For *in vitro* reconstitutions, this viscous relaxation is thought to result from transient unbinding and rebinding of intermolecular cross-links[?, ?]. However, there is still no clear understanding of how local relaxations of network connectivity would give rise to a global viscous relaxation. In our work, we wish to expand upon a well-established mechanical picture of cross-linked semi-flexible polymer networks to incorporate slippage of cross-links over longer timescales.

1.1.1 *Short Timescale Mechanics of Cross-linked Actin Filament Networks*

Early *in vitro* studies of cross-linked actin filament networks revealed strikingly different elastic behaviors compared to the already well-understood flexible polymer gels [?]. The complexity of these behaviors drove a surge in both experimental and theoretical studies of semi-flexible networks. For a comprehensive review of this field we recommend [?], but we will shortly repeat some important milestones here.

Theories of Semi-flexible Filament Networks

Diversity and discrepancy in observations led a drive toward systematic *in vitro* experimental explorations of the rheology of cross-linked semi-flexible polymer networks at short timescales. In studies with rigid irreversibly cross-linked networks, it was found that differences in network structure could lead to remarkably different elastic moduli, suggesting distinct phases of mechanical response [?]. These discoveries in turn begat theoretical work on the basic implications of the semi-flexible nature of filaments on network mechanics.

Prior work on the basic physics of individual semi-flexible polymers [?, ?], and comprehensive theories of semi-flexible filament solutions, [?] laid a groundwork for theoretical considerations of cross-linked networks. Beginning with the so-called "mikado model" descriptions[?, ?], it was determined that there should exist a minimum rigidity percolation threshold, and that the connectivity of the network determined whether the mechanical response was dominated by non-affine bending or affine stretching of filaments. Continuing to more explicit theories[?], the mechanics of rigidly cross-linked networks were shown to be well-described in terms of purely elastic stretching of filaments between cross-linked points.

Incorporating Effects of Cross-link Compliance

Despite the success of the theory for rigid cross-links, early studies showed that surprising qualitative differences in mechanical response could be traced to differences in the chosen cross-linker[?, ?]. In addition, many studies using more compliant cross-linkers showed that cross-linker compliance could give rise to different nonlinear rheological properties on short timescales[?, ?, ?, ?]. Making matters even more complicated, ongoing research has begun to uncover added complexity from more highly complex issues such as filament bundling[?, ?]and the effects of active cross-linking by molecular motors[?].

While theorists have built a number of largely successful models that help characterize different aspects of the cross-link dominated response[?, ?, ?], the diversity of behaviors of these networks makes a precise yet general theory more difficult.

1.1.2 Long Timescale Stress Relaxation from Transient Cross-link Unbinding

At long timescales, the purely elastic behavior of cross-linked networks gives way to fluid-like stress relaxation. Additionally, fluid-like flows have been observed in a number of cellular processes[?, ?, ?, ?, ?, ?]. In *in vitro* studies, long timescale creep behaviors are thought to arise predominantly from the transient nature of filament binding for most biologically relevant cross-linkers[?, ?, ?, ?]. While the importance of cross-link dynamics in determining the mechanical response of semi-flexible polymer networks has been known for at least 20 years[?], there is still a gap in our understanding of how microscopic cross-link unbinding relates to viscous flows.

Models of Stress Relaxation with Transient Cross-links

The dependence of network rheology on cross-link unbinding is an active subject of theoretical research[?].

Several theoretical methods have addressed cross-link binding and unbinding directly [?, ?] in analytical approaches that allowed well-constrained fits for specific cross-linkers. These theories have therefore focused conceptually at the level of the cross-linked filament and were extended analytically to macroscopic networks. In another approach, modelers have taken cross-links as extended springlike structures [?] that are able to bind and unbind in simulated filament networks. Finally, other more ambitious simulations have even sought to interrogate the effects of cross-link unbinding in combination with the more complex mechanics of filament bundles[?, ?].

Ultimately, the complexity of the many theoretical approaches that have been applied to this problem have made it difficult to distinguish what, if any, core physical mechanisms may be sufficient to explain the observed forms of stress relaxation. We believe that serious qualitative understanding can be generated by focusing on some of the common elements exhibited in the aforementioned literature.

Novelty of Cross-link Slip Approach

Here, we introduce a coarse-grained representation of filament cross-linking in which cross-linked filaments which are able to slide past each other as molecular bonds form and rupture, akin to coarse-grained models of molecular friction[?, ?, ?]. This drag-like coupling has been shown to be an adequate approximation in the case of ionic cross-linking of actin[?, ?], and can be found in the theoretical basis of force-velocity curves for myosin bound filaments[?]. We propose that it will form a suitable bulk approximation in the presence of super molecular cross-links as well.

Importantly, this simplification allows us to extend our single polymer models to dynamical systems of larger network models for direct comparison between theory and modeling results. This level of coarse graining will therefore make it easier to understand classes of behavior for varying compositions of cross-linked filament networks. In addition, it allows us to compute a new class of numerical simulations efficiently, which gives us concrete predictions for behaviors in widely different networks with measurable dependencies on molecular details.

1.2 Introduction

Cortical flow is a fundamental and ubiquitous form of cellular deformation that underlies cell polarization, cell division, cell crawling and multicellular tissue morphogenesis[?, ?]. These flows arise within the actomyosin cortex, a thin layer of cross-linked actin filaments and myosin motors that lies just beneath the plasma membrane [?]. The active forces that drive cortical flows are thought to be generated by myosin motors pulling against individual actin filaments [?]. These forces must be integrated within cross-linked networks to build macroscopic contractile stress. At the same time, cross-linked networks resist deformation and this resistance must be dissipated by network remodeling to allow macroscopic network deformation and flow. How force production and dissipation depend on motor activity, network architecture and remodeling remains poorly understood.

Current models for cortical flow rely on coarse-grained descriptions of actomyosin networks as active fluids, whose motions are driven by gradients of active contractile

stress and opposed by an effectively viscous resistance[?]. In these models, gradients of active stress are assumed to reflect spatial variation in motor activity and viscous resistance is assumed to reflect the internal dissipation of elastic resistance due to local remodeling of filaments and/or cross-links [?]. A key virtue of these models is that their behavior is governed by a few parameters (active stress and effective viscosity). By coupling an active fluid description to simple kinetic models for network assembly and disassembly and making active stress and effective viscosity depend on e.g network density and turnover rates, it is possible to capture phenomenological descriptions of cortical flow. Models based on this active fluids description can successfully reproduce spatiotemporal dynamics of cortical flow observed during polarization [?], cell division [?, ?], cell motility [?, ?] and tissue morphogenesis [?].

However, to understand how cells exert physiological control over cortical deformation and flow, or to build and tune networks with desired properties *in vitro*, it is essential to connect this coarse-grained description to the microscopic origins of force generation and dissipation within cross-linked actomyosin networks. Both active stress and effective viscosity depend sensitively on microscopic parameters including densities of filaments, motors and cross-links, force-dependent motor/filament interactions, cross-link dynamics and network turnover rates. Thus a key challenge is to understand how tuning these microscopic parameters controls the dynamic interplay between active force generation and passive relaxation to control macroscopic dynamics of cortical flow.

Studies in living cells have documented fluid-like stress relaxation on timescales of 10-100s of seconds [?, ?, ?, ?, ?, ?]. These modes of stress relaxation are thought to arise both from the transient binding/unbinding of individual cross-links and from the turnover (assembly/disassembly) of actin filaments (ref). Studies of cross-linked and/or bundled actin networks *in vitro* suggest that cross-link unbinding may be sufficient to support viscous relaxation (creep) on very long timescales[?, ?, ?, ?, ?], but is unlikely to explain the rapid large scale cortical deformation and flow observed in living cells. It has been proposed in the field that rapid actin turnover must play a significant role as well. Indeed, photokinetic and single molecule imaging studies studies

reveal rapid turnover of cortical actin filaments in living cells on timescales of 10-100 seconds [?]. Previous theoretical models have explored the dependence of stress relaxation on cross-link binding and unbinding analytically [?, ?] and others have explicitly modeled reversible cross-linking in combination with complex mechanics of filament bundles [?, ?, ?], leading to complex viscoelastic stress relaxation. However, until very recently [?] very little attention has been paid to actin turnover as mechanism of stress relaxation.

Recent work has also begun to reveal insights into mechanisms that govern active stress generation in disordered actomyosin networks. In vitro studies have confirmed that local interactions among actin filaments and myosin motors are sufficient to drive macroscopic contraction of disordered networks [?]. Theoretical studies suggest that asymmetrical compliance of actin filaments (stiffer under extension than compression) and spatial differences (dispersion) in motor activity are sufficient conditions for contraction in one [?] and two [?] dimensional networks, although other routes to contractility may also exist [?]. Further work has explored how modulation of network architecture, cross-link dynamics and motor density, activity and assembly state can shape rates and patterns of network deformation [?, ?, ?] or network rheology [?, ?].

Significantly, *in vitro* models for disordered actomyosin networks have used stable actin filaments, and these networks support only transient contraction, either because of network collapse[?], or buildup of elastic resistance[?], or because network rearrangements (polarity sorting) dissipate the potential to generate contractile force [?, ?]. This suggests that continuous turnover of actin filaments may play a key role in allowing sustained deformation and flow. Recent theoretical and modeling studies have begun to explore how this could work [?, ?, ?], and to explore dynamic behaviors that can emerge in contractile material with turnover [?]. However, there is much to learn about how the buildup and maintenance of contractile force during continuous deformation and flow depends on the local interplay of network architecture, motor activity and filament turnover.

The goal of this work is to build a computational bridge between the microscopic description of cross-linked actomyosin networks and the coarse grained macroscopic

description of an active fluid. We seek to capture the essential microscope features (dynamic cross-links, active motors and semi flexible actin filaments with asymmetric compliance and continuous filament recycling), but in a way that is sufficiently simple to allow systematic exploration of how parameters that govern network deformation and flow in an active fluid theory depend on microscopic parameters. To this end, we introduce several coarse-grained approximations into our representation of filament networks. First, we represent semi-flexible actin filaments as simple springs with asymmetric compliance (stronger in extension than compression). Second, we replace dynamic binding/unbinding of elastic cross-links with a coarse-grained representation in terms of molecular friction [?, ?, ?], such that filaments can slide past each other against a constant fictional resistance. Third, we used a similar scheme to introduce active motors at filament crossover points with a simple linear force/velocity relationship, and we introduce dispersion of motor activity by making only a subset of filament overlaps active [?]. Finally, we model filament turnover by allowing entire filaments to appear and disappear with a fixed probabilities per unit time. Importantly, these simplifications allow us to extend our single polymer models to dynamical systems of larger network models for direct comparison between theory and modeling results. This level of coarse graining will therefore make it easier to understand classes of behavior for varying compositions of cross-linked filament networks. In addition, it allows us to compute a new class of numerical simulations efficiently, which gives us concrete predictions for behaviors in widely different networks with measurable dependencies on molecular details.

CHAPTER 2
IMPACT OF FILAMENT RECYCLING ON CORTICAL
FLOW IN ANIMAL CELLS

CHAPTER 3

MODELING 2D ACTIVE NETWORKS WITH RECYCLING

3.1 Models

Our motivation is to model essential microscope features of cross-linked actomyosin networks (semi flexible actin filaments with asymmetric compliance, dynamic cross-links, active motors and and continuous filament recycling), in a way that is simple enough to allow systematic exploration of how tuning these microscopic features controls macroscopic network deformation and flow. We focus on 2D networks for computational tractability and because they capture a reasonable approximation of the quasi-2D cortical actomyosin networks that govern flow and deformation in many eukaryotic cells[?, ?], or the quasi-2D networks studied recently in vitro[?, ?].

3.1.1 Asymmetric filament compliance

We model individual filaments as chains of springs with relaxed length l_s . Filaments can therefore be represented as a sequence of nodes with positions \mathbf{x}_i , where the index i enumerates over all nodes of all segments. The internal elastic resistance of filament segments gives rise to nearest neighbor force interactions, $\mathbf{F}_{i,i+1}^\mu$, of the form

$$\mathbf{F}_{i,i+1}^\mu = \mu \frac{|\mathbf{x}_{i+1} - \mathbf{x}_i| - l_s}{l_s} \left(\frac{\mathbf{x}_{i+1} - \mathbf{x}_i}{l_s} \right) \quad (3.1)$$

where the modulus, μ , is a composite quantity representing both filament and cross-linker compliance in a manner similar to a proposed effective medium theory [?]. To model asymmetric filament compliance, we assign a different value to the modulus μ , depending on whether the strain on a given filament segment, $(|\mathbf{x}_{i+1} - \mathbf{x}_i| - l_s)/l_s$, is greater or less than 0. In the limit of highly rigid cross-links and flexible filaments,

our model reduces to the pure semi-flexible filament models of [?, ?]. In the opposite regime of nearly rigid filaments and highly flexible cross links, our model is essentially the same as that of [?] in small strain regimes before any nonlinear cross link stiffening. In a departure from those previous models, we assume here that the magnitude of the force on interior cross-links is the same as those on the exterior. This approach ignores the variation in strain on these two sets of cross-links as addressed in [?], but we choose to ignore this variation in favor of an approximated, global mean approach.

Because we are dealing with semi-flexible filaments we also introduce a bending modulus between our filament segments such that the restoring force is proportional to the angle between the filament segments and points in the direction orthogonal to the filament direction, $\mathbf{u}_i = (\mathbf{x}_{i-1} - \mathbf{x}_i)/|\mathbf{x}_{i-1} - \mathbf{x}_i|$.

The total internal force on a filament node i can therefore be written as:

$$\mathbf{F}_i^{\text{int}} = \mathbf{F}_{i-1,i}^\mu + \mathbf{F}_{i,i+1}^\mu \quad (3.2)$$

Introducing a filament bending stiffness adds another mode of asymmetric compliance since filaments can bend/buckle internally under compression. For the majority of the work presented here, we have set $l_s = L$ to obviate dependence on bending driven asymmetries. However, as shown in supplemental figure xxx (TBA) the major points of the paper are still valid for $l_s < L$ under the condition that $\kappa/l_s \gg \mu_c$.

3.1.2 Drag-like coupling between overlapping filaments

Previous models represent cross-linkers as elastic connections between pairs of points on neighboring filaments that appear and disappear with either fixed or force-dependent probabilities [?, ?]. Here, we introduce a simpler coarse-grained model for dynamic cross-links by replacing many transient elastic interactions with an effective drag-like coupling between every pair of overlapping segments.

$$\mathbf{F}_{i-1,i}^\xi = \xi \sum_j \frac{l_s - |s_{ij} - s_i|}{l_s} (\mathbf{v}_{i-1,i} - \mathbf{v}_{j-1,j}) \quad (3.3)$$

where $\mathbf{v}_{n-1,n}$ represent the average velocity of the filament segment spanning nodes

$n - 1$ and n , and the sum is taken over all filament segments such that the segment from node $j - 1$ to node j intersects the segment from $i - 1$ to i at the location s_{ij} .

$$\mathbf{F}_i^{\text{coup}} = \mathbf{F}_{i-1,i}^\xi + \mathbf{F}_{i,i-1}^\xi \quad (3.4)$$

This model assumes a linear relation between the drag force and the velocity difference between attached segments. This drag-like coupling has been shown to be an adequate approximation in the case of ionic cross-linking of actin[?, ?], and can be found in the theoretical basis of force-velocity curves for myosin bound filaments[?]. Although non-linearities can arise through force dependent detachment kinetics and/or non-linear force extension of cross-links, we assume that inhomogeneities from non-linear effects are of second or higher order. With this assumption, the motion of filaments can be described by a deterministic dynamical equation of the form

$$0 = -l_s \zeta \mathbf{v}_i - \mathbf{F}_i^{\text{coup}} + \mathbf{F}_i^{\text{int}} \quad (3.5)$$

Here, the first term is the filament's intrinsic drag through its embedding fluid, ζ , while the second comes from the drag-like coupling between filaments, ξ .

3.1.3 Active coupling for motor driven filament interactions

To add motor activity we select a subset of cross-linked points and impose an additional force of magnitude v on each of the overlapping filament segments, directed towards the (+) end of that segment, $\mathbf{u}_i = (\mathbf{x}_{i-1} - \mathbf{x}_i)/|\mathbf{x}_{i-1} - \mathbf{x}_i|$. Thus, the total “active” force on a given filament segment is

$$\mathbf{F}_{i-1,i}^v = v \mathbf{u}_i \sum_j \frac{l_s - |s_{ij} - s_i|}{l_s} q_{ij} \quad (3.6)$$

where q_{ij} equals 0 or 1 depending on whether there is an “active” cross-linker at this location. To model dispersion of motor activity, we set $q_{ij} = 1$ on a randomly selected subset of cross-link points, such that $\bar{q} = \phi$, where \bar{q} indicates the mean of q .

Finally, for each active force, $\mathbf{F}_j^{\text{act}}$, imparted by filament j , we must also impart the opposite force onto the filament between i and $i + 1$ as well. Therefore, the entire

equation for activity will appear as

$$\mathbf{F}_i^{\text{act}} = \mathbf{F}_{i-1,i}^v + \mathbf{F}_{i,i+1}^v - \sum_j \mathbf{F}_{j-1,j}^v q_{ij} \quad (3.7)$$

This will leave us with a full equation of motion given by the sum of each of the parts defined above.

$$0 = -L\zeta \mathbf{v}_i - \mathbf{F}_i^{\text{coup}} + \mathbf{F}_i^{\text{int}} + \mathbf{F}_i^{\text{act}} \quad (3.8)$$

3.1.4 2D network formation

We used a mikado model approach [?] to initialize a minimal network of connected unstressed linear filaments in a rectangular 2D domain. We generate 2D networks of these semi-flexible filaments by laying down straight lines of length, L , with random position and orientation. We then assume that overlapping filaments become cross-linked at their points of overlap. Although real cytoskeletal networks may form with non-negligible anisotropy, for simplicity, we focus on isotropically initialized networks. We define the density using the average distance between cross-links along a filament, l_c . A simple geometrical argument can then be used to derive the number of filaments filling a domain as a function of L and l_c [?]. Here, we use the approximation that the number of filaments needed to tile a rectangular domain of size $D_x \times D_y$ is $2D_x D_y / L l_c$, and that the length density is therefore simply, $2/l_c$. In the absence of cross-link slip, we expect the network to form a connected solid with a well defined elastic modulus[?, ?].

3.1.5 External applied stress

We can model our active networks as a coupled system of differential equations satisfying 3.8. However, to probe the passive response of the network, we also wish to incorporate externally applied stresses. Although the general passive mechanical response of this system may be very complex, we focus our attention on low frequency deformations and the steady-state creep response of the system to an applied stress.

To do this we introduce a fixed stress, σ along a fixed domain at one edge of the network. The stress is applied via individual forces to the filaments lying within a patch of size D_w such that the sum of individual forces is equal to the applied stress times the height of the domain. These forces point in the direction, $\hat{\mathbf{x}}$, producing an extension of the patch. The region of applied stress does not move as the network deforms, allowing us to more easily focus our attention on a fixed sized domain.

Finally, we add a 0 velocity constraint at the other edge of our domain of interest. We assume that our network is in the “dry,” low Reynold’s number limit, where inertial effects are so small that we can equate our total force to 0. Therefore, we have a dynamical system of wormlike chain filaments satisfying

$$0 = -L\zeta\mathbf{v}_i - \mathbf{F}_i^{\text{coup}} + \mathbf{F}_i^{\text{int}} + \mathbf{F}_i^{\text{act}} + \sigma\hat{\mathbf{u}}(\mathbf{x}_i) \quad (3.9)$$

subject to constraints such that $\mathbf{v}_i(\mathbf{x})$ is 0 with $x = 0$. This results in an implicit differential equation for filament segments which can be discretized and integrated in time to produce a solution for the motion of the system.

3.1.6 Modeling filament turnover

In living cells, actin filament assembly is governed by multiple factors that control nucleation, elongation and filament branching. Likewise filament disassembly is governed by multiple factors that promote filament severing and monomer dissociation at filament ends. Here, we focus on a lowest order model for filament recycling in which entire filaments appear with a fixed rate per unit area, k_{app} and disappear at a rate $k_{diss}\rho$, where ρ is a filament density. With this assumption, in the absence of network deformation, the density of filaments will equilibrate to a steady state density, k_{app}/k_{diss} , with time constant $\tau_r = 1/k_{diss}$. In deforming networks, the density will be set by a competition between strain thinning ($\gamma > 0$) or thickening ($\gamma < 0$), and density equilibration via turnover. To implement this assumption, at fixed time interval $\tau_s < 0.01 \cdot \tau_r$ (i.e. 1% of the equilibration time), we selected a fraction, τ_s/τ_r , of existing filaments (i.e. less than 1% of the total filaments) for degradation. We then generated a fixed number of new unstrained filaments $k_{app}\tau_s D_x D_y$ at random

positions and orientations within the original domain. We refer to this continuous turnover as filament recycling, to $k_{diss} = 1/\tau_r$ as the recycling rate, and to τ_r as the recycling time.

3.1.7 *Simulation methods*

Details of our simulation approach can be found in the Appendix. Briefly, equations 3.1, 3.4, 3.6 and 3.9 define a coupled system of ordinary differential equations for the velocities of the endpoints of filament segments, $\dot{\mathbf{x}}$. These equations are coupled by the effective cross-link friction on segment overlap points, yielding a system of the form:

$$\mathbf{A} \cdot \dot{\mathbf{x}} = \mathbf{f}(\mathbf{x}) \quad (3.10)$$

where \mathbf{A} represents a coupling matrix between endpoints of filaments that overlap, and $\mathbf{f}(\mathbf{x})$ is the spring force between pairs of filament segment endpoints. We numerically integrate this system of equations to find the time evolution of the positions of all filament endpoints. We generate a network of filaments with random positions and orientations as described above within a domain of size D_x by D_y . For all simulations, we imposed periodic boundaries in the y-dimension. To impose an extensional stress, we constrained all filament segment endpoints within a fixed distance $0.05 \cdot D_x$ from the left edge of the domain to be non-moving, then we imposed a rightwards force on all segment endpoints within a distance $0.05 \cdot D_x$ from the left edge of the patch. To simulate free contraction, we removed all constraints at boundaries; to assess buildup of contractile stress under isometric conditions, we pinned both left and right edges of the network as described above.

We smoothed all filament interactions, force fields, and constraints over small regions such that the equations contained no sharp discontinuities. The nominal units for length, force, and time are μm , nN, and s, respectively. We explored parameter space around an estimate of biologically relevant parameter values given in Table 3.1.

Table 3.1: Simulation Parameter Values

parameter	symbol	physiological estimate
extensional modulus	μ_e	$1nN$
compressional modulus	μ_c	$0.01nN$
cross-link drag coefficient	ξ	<i>unknown</i>
solvent drag coefficient	ζ	$0.0005\frac{nNs}{\mu m^2}$
filament length	L	$5\mu m$
cross-link spacing	l_c	$0.5\mu m$
domain size	$D_x \times D_y$	$20 \times 50\mu m$

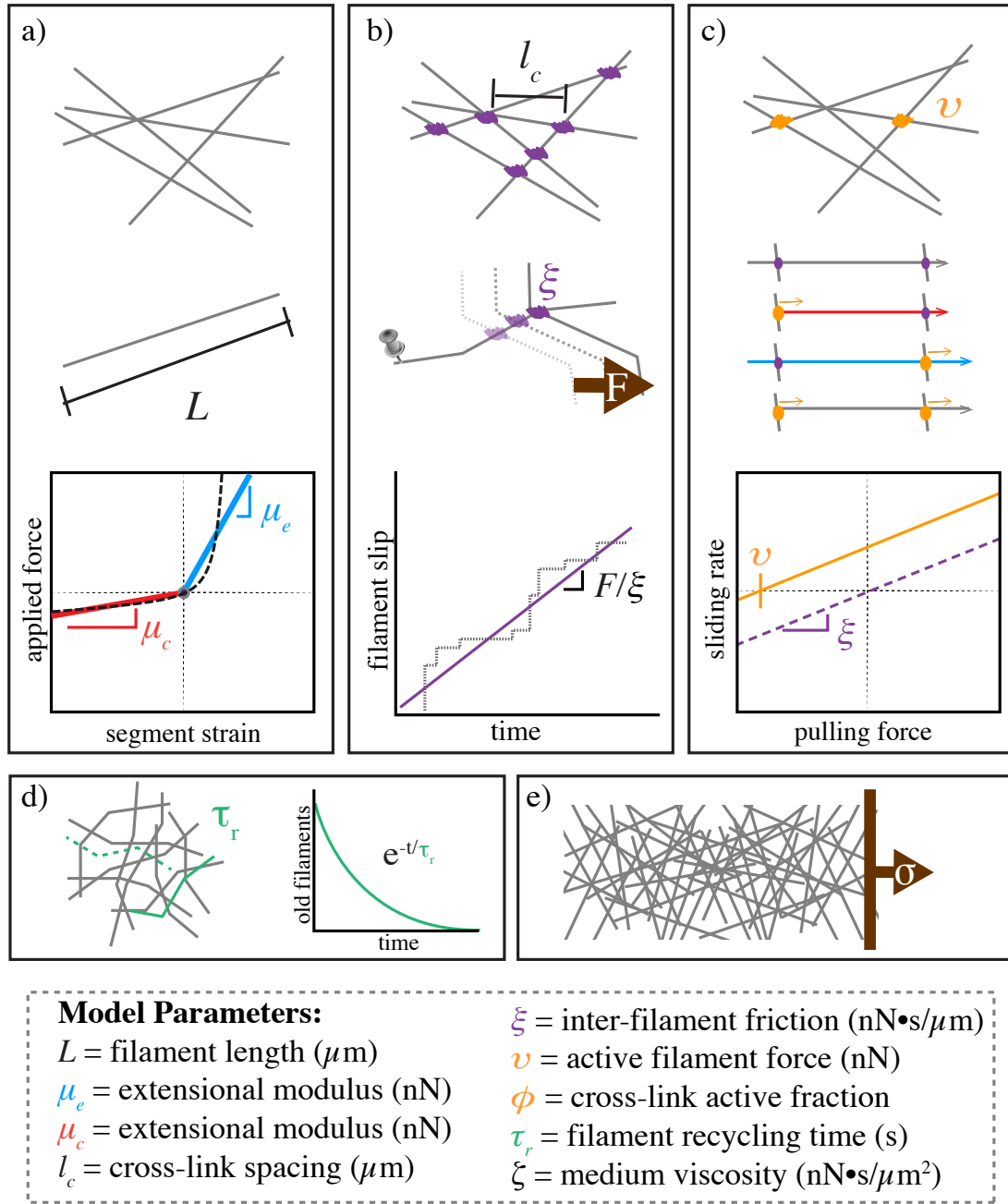


Figure 3.1: Schematic of modeling framework. a) Asymmetric filament compliance. Filaments have smaller spring constant for compression than for extension. b) Cross-link slip. Cross-links are coupled by an effective drag, such that their relative motion is proportional to any applied force. c) Motor activity. Filament activity manifests as a basal sliding rate even in the absence of an external force. Fractional activity. Only a subset of filament cross-links are active, resulting in differential force exertion along the filament. d) Filament recycling. Filaments are turned over at a constant rate, leading to a refreshing in the strain state of all filaments after a characteristic timescale. e) Applied stress. In simulations with passive cross-links, and external stress is applied as force field acting on a fixed spatial domain.

CHAPTER 4

FILAMENT RECYCLING AND SUSTAINED CONTRACTILE FLOWS IN AN ACTOMYOSIN NETWORK

4.1 Results and Discussion

We aim to characterize how rates and patterns of cortical flow are shaped by complex dependencies of active stress generation and passive stress dissipation on network architecture, local coupling (active and passive) between filaments and filament recycling. We approached this in three steps: First, we analyzed the passive deformations of cross-linked networks (absent active motors) in response to a constant external force. Then, we analyzed the dynamics of internal stress buildup and dissipation in the same networks, but with active motors, as they contract freely or build force against fixed external boundaries. Finally, we consider the dynamic interplay of internal stress buildup, contraction, and stress relaxation in networks that undergo steady state flow in response to spatial gradients of motor activity.

4.1.1 Filament recycling prevents cortical tearing and modulates the viscous stress relaxation of passive filament networks

Networks with passive cross-links and no filament turnover undergo three stages of deformation in response to an extensional force. To characterize the passive response of a cross-linked filament network in the absence of filament recycling and motor activity, we imposed an external force on the simulated network, and then quantified the mechanical response in terms of internal network stress and network strain as a function of time. Figure 4.1a shows the typical response of a simulated network. We measured the local velocity of the network at different

positions along the axis of deformation as the mean velocity of all filament segments intersecting that position; we measured the internal network stress at each position by summing the axial component of the tensions on all filament segments intersecting that position, and dividing by network height; finally, we measured network strain rate as the average of all filaments velocities divided by their positions.

During early (not shown) and intermediate (Figure 4.1b) stages of the deformation, the internal stress (blue) was nearly constant throughout the material while the velocity (orange) increased linearly with distance from the site of network attachment, indicating an approximately uniform deformation (strain) rate throughout the material. Accordingly, we report the network response in terms of time-dependent bulk material stress and strain.

Plotting the bulk stress and strain as a function of time revealed that the deformation occurred in three qualitatively distinct phases (Figure 4.1a,c). On short timescales the response was viscoelastic, with a rapid buildup of internal stress and a rapid \sim exponential approach to a fixed strain, which represents the elastic limit in the absence of cross-link slip predicted by [?]. On intermediate timescales, the internal stress remained constant while the network continued to deform slowly and continuously with nearly constant strain rate (shown as dashed line in Fig 4.1c) as filaments slipped past one another against the effective cross-link drag. This linear relationship between strain and time characterizes a material with an effective viscosity, η , given by the ratio of the applied stress to the strain rate. We define the transition time between the fast, viscoelastic phase and the slower, effectively viscous deformation phase as τ_c . Finally, as the network strain approached a critical value ($\sim 30\%$ for the simulation in Figure 4.1), strain thinning led to decreased network connectivity, local tearing, and acceleration of the network deformation (see inset in Figure 4.1c), eventually resulting in the highly heterogeneous network structure shown in the $t=440s$ example of Figure 4.1a.

Network architecture sets the rate and timescales of deformation. To better understand how network architecture and cross-link dynamics control effective viscosity and the timescale for transition to viscous behavior, we systematically varied

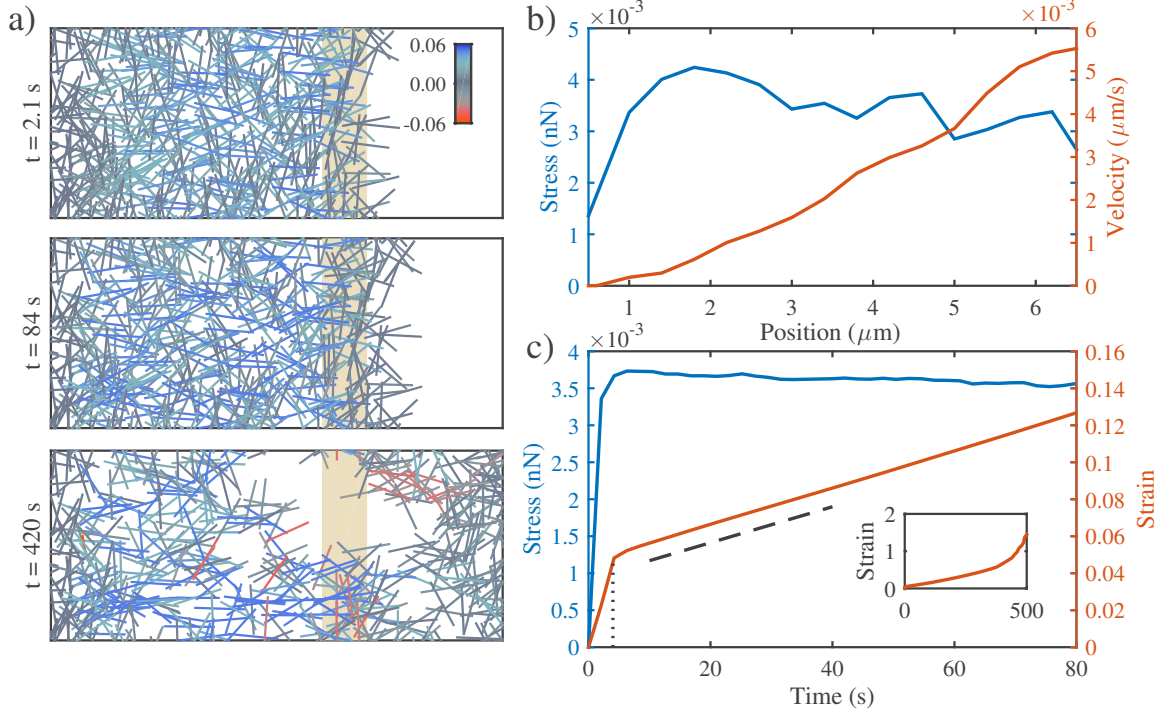


Figure 4.1: Networks with passive cross-links and no filament turnover undergo three stages of deformation in response to an extensional force. **a)** Three successive time points from a simulation of a $4 \times 6.6 \mu\text{m}$ network deforming under an applied extensional stress of $0.005 \text{ nN}/\mu\text{m}$ (stress is applied to filaments in the region indicated by the tan bar). Network deforms to a final dimension of $\sim 4 \times 10 \mu\text{m}$. In this and all subsequent figures, filaments are color-coded with respect state of strain (blue = tension, red = compression). Network parameters: $L = 1 \mu\text{m}$, $l_c = 0.3 \mu\text{m}$, $\xi = 100 \text{ nN} \cdot \text{s}/\mu\text{m}$. **b)** Mean filament stress and velocity profiles for the network in (a) at $t=88$ s. Note that the stress is nearly constant and the velocity is nearly linear as predicted for a viscous fluid under extension. **c)** Plots of the mean stress and strain vs time for the simulation in (a), illustrating the three stages of deformation: (i) A fast initial phase accompanies rapid buildup of internal network stress; (ii) after a characteristic time τ_c (indicated by vertical dotted line) the network deforms like a material with a constant effective viscosity, η_c , as indicated by the slope of the dashed line; (iii) at long times, the strain accelerates (see inset) as the network undergoes strain thinning and eventually tears.

network parameters (see S1 Table), and measured the elastic modulus, G_0 , effective viscosity, η , and transition time, τ_c , in response to a fixed external stress. We observed the transition from a viscoelastic to an effectively viscous phase for the entire

range of parameters that we sampled. The elastic limit that we observe during the viscoelastic phase agreed closely with the closed form solution for the elastic modulus $G_0 \sim \mu/l_c$ predicted by a previous model [?] for networks of semi-flexible filaments with irreversible cross-links (Mechanical properties of passive networks. **a)** Elastic modulus of networks. Our measurements closely match prediction of $G_0 \sim \mu/l_c$. **b)** Placeholder for inevitably another figure relevant to passive properties). A simple theoretical analysis (shown in S1 Text) predicts that in the viscous phase, the effective viscosity should be proportional to the cross-link drag coefficient and to the square of the number of cross-links per filament, with a constant of proportionality $\pi/4$. We define this predicted scaling of effective viscoisty as η_c .

$$\eta_c = \frac{\pi}{4} \xi \left(\frac{L}{l_c} - 1 \right)^2 \quad (4.1)$$

As shown in Figure 4.2a, our simulations agree well with this prediction for a large range of network parameters. For many linear viscoelastic materials, the ratio of the viscosity, η_c , to the elastic modulus, G_0 , is a general indicator of the transition timescale from elastic to viscous behavior[?]. Using our approximations of the elastic modulus and viscosity, we predict a crossover time, $\tau_c \approx L^2 \xi / l_c \mu$. By measuring the time at which the strain rate became nearly constant (i.e $\dot{\gamma} \sim t^n$ with $n > 0.8$) we obtained an estimate of this time for a wide variety of simulation parameters. As shown in Figure 4.2b, our approximation is in good agreement with the observed transition time, indicating that the passive responses of our simulated networks are well represented by effectively linear bulk properties, at least over small strains.

Filament recycling rescues network tearing and modulates effective viscosity. To explore how filament recycling shapes the passive network response to an applied force, we ran a series of simulations with identical filament lengths and network densities and cross-link drag coefficients, while varying the filament recycling time $\tau_r = 1/k_{diss}$. Figure 4.3a illustrates the results for a particular set of network parameters. In the absence of filament recycling, strain thinning and network tearing lead to a rapid increase in strain rate above a critical strain of $\sim 40\%$.

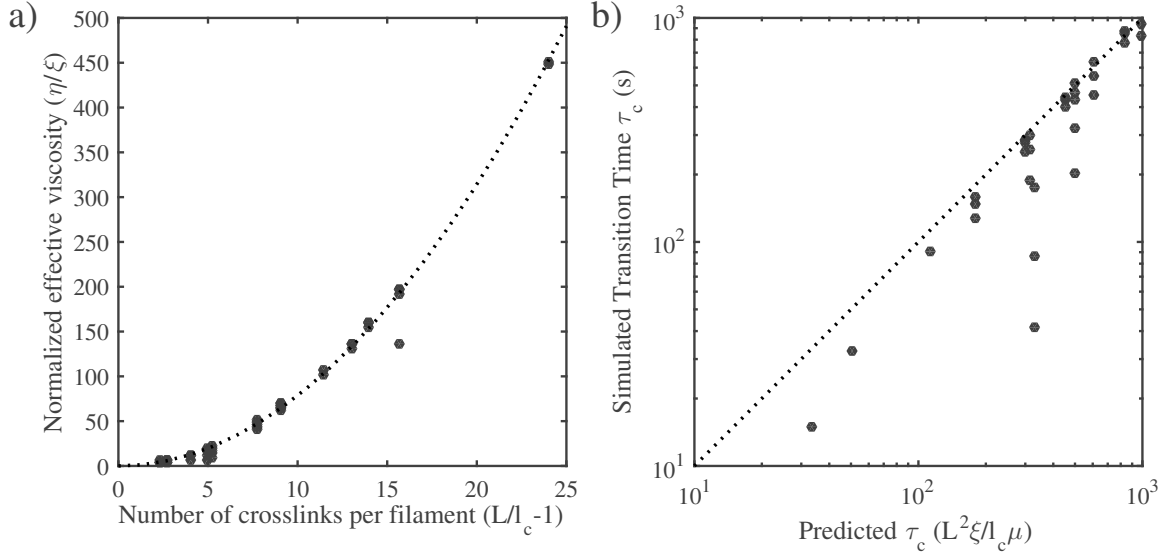


Figure 4.2: Network architecture sets the rate and timescales of deformation. **a)** The effective viscosity depends on the drag coefficient and the density of the network. Data points are the normalized effective viscosities from simulations (effective viscosity measured in fluid phase divided by the cross link friction coefficient) vs the number of cross links per filament ($L/l_c - 1$). Dotted line indicates the relationship predicted by a simple theory, $\eta_c = \xi(L/l_c - 1)^2$ **b)** The transition to viscous behavior occurs at a characteristic time, τ_c .

Progressively decreasing the filament recycling time led to a progressive increase in the rate of network deformation during the effectively viscous phase and an increase in the critical strain at which the network began to tear. As we decreased the recycling time below a critical recycling time (τ_{crit}), the networks began to sustain effectively viscous deformation indefinitely, as shown by the lack of strain thinning in the strain profiles of (ANOTHER SUPPLEMENTAL FIGURE). Intuitively, steady state deformation is achieved when the rate of filament depletion by strain thinning is balanced by a sufficiently high rate of filament recycling (i.e. a sufficiently low recycling time). To determine the critical recycling time, we write an equation for the rate of change in filament density ρ , as a function of filament recycling ($k_{app} - k_{diss}\rho$) and strain thinning ($-\dot{\gamma}\rho$). These terms can be rewritten to give the following

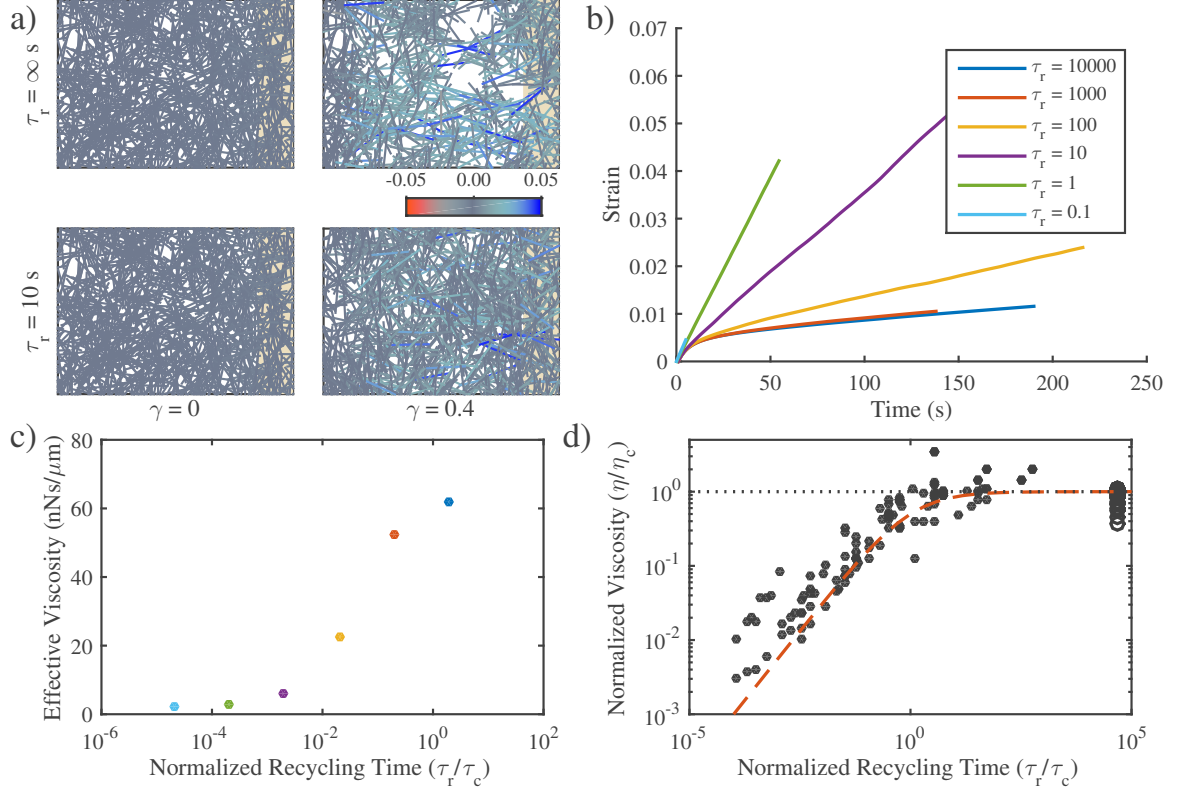


Figure 4.3: Filament recycling modulates effective viscosity in two regimes. **a)** Examples of $20 \times 12 \mu m$ network under $0.001 \text{ nN}/\mu m$ extensional stress with recycling ($\tau_r = 10 \text{ s}$) and without, ($\tau_r = \infty$). Both images are taken when the patches had reached a net strain of 0.4. The network with recycling doesn't appear to change shape because its components have been recycled to remain in the original domain. Network parameters: $L = 3 \mu m$, $l_c = 0.5 \mu m$, $\xi = 10 \text{ nN} \cdot \text{s}/\mu m$. **b)** Strain curves for identical networks with varying levels of filament recycling. Network parameters: $L = 3 \mu m$, $l_c = 0.5 \mu m$, $\xi = 10 \text{ nN} \cdot \text{s}/\mu m$. **c)** Plotting the effective viscosity derived from the slopes of the lines in panel a. **d)** Effective viscosities (normalized by the effective viscosity in the absence of recycling, η_c) as a function of the normalized recycling time. When the recycling timescale is significantly less than the passive relaxation timescale, the viscosity of the network becomes dependent on recycling time. Red dashed line indicates the approximation given in equation 4.3 for $m = 3/4$.

$$\frac{d\rho}{dt} = \frac{\rho_0 - \rho}{\tau_r} - \frac{\sigma}{\eta_c(\rho)}\rho \quad (4.2)$$

where k_{diss} has been replaced by $1/\tau_r$, and $\rho_0 = k_{app}\tau_r$, and $\dot{\gamma}$ has been replaced by

σ/η_c . For our networks, the effective viscosity, η_c , is dependent on the filament density (through l_c) so this dependence must be included. Solving this equation for its steady states, and replacing the initial density, ρ_0 , with the length density approximation, $2/l_c$, we find that a constant steady state density only exists under the condition $\tau_r < \tau_{crit} = \eta_c/2\sigma$.

Reducing recycling time, τ_r , below τ_{crit} produced different effects on steady state deformation rates depending on the relative values of τ_r and τ_c , the characteristic time for the transition to effectively viscous deformation in the absence of recycling. For $\tau_r > \tau_c$, the deformation rate is dominated by cross-link resistance to sliding of strained filaments, and the effective viscosity remained \sim constant with decreasing τ_r ; for $\tau_r < \tau_c$, effective viscosity decreased sublinearly with decreasing τ_r . Intuitively, this is because, for $\tau_r < \tau_c$, the deformation rate is limited by the level of elastic stress on partially strained filaments; By replacing partially strained with unstrained filaments, the network is able to tune the mean level of stress and thus the deformation rate.

To confirm this relationship more generally, we allowed filament lengths, network density and cross link friction to vary more widely, and we measured the network deformation rates while varying filament recycling times (Figure 4.3a,b). We then plotted the normalized effective viscosity (ratio of effective viscosity with recycling to effective viscosity without recycling, η_c) vs a normalized recycling rate (recycling time scaled by τ_c). Indeed, we found that the normalized effective viscosity measured during steady state flow begins to decrease when the recycling time falls below τ_c and below this value the effective viscosity falls off nearly linearly with recycling time to minimal values (Figure 4.3c).

To describe this we introduce (based on linear viscoelastic models of [?]) an effective recycling viscosity, η_r , which can be tuned between the τ_r dependent and independent regimes, depending on the value of the recycling timescale.

$$\eta_r = \frac{\eta_c}{1 + (\tau_c/\tau_r)^m} \quad (4.3)$$

For $\tau_r \gg \tau_c$, this simplifies to $\eta_r \approx \eta_c$, while for $\tau_r \ll \tau_c$, this simplifies to

$\eta_r \sim (\tau_r/\tau_c)^m$, which matches with our measurements as found in Figure 4.3d for a large range of parameters (with $m = 3/4$). While the origins of the $3/4$ scaling remain unclear, this model captures a simple quantitative description of our simulation data.

In summary, our simulations predict that tuning recycling times below a critical value τ_{crit} , allows networks to undergo continuous viscous deformation, for long times, without tearing, for a wide range of different effective viscosities and deformation rates. Given a suitably low strain rate, τ_{crit} will be substantially larger than the other timescales of interest. For $\tau_r < \tau_{crit}$, modulating filament recycling times can tune the network between two regimes. For $\tau_r > \tau_c$, the deformation is limited by effective cross-link friction. The effective viscosity depends on the strength of inter-filament cross-linking and the network's architecture, and is relatively insensitive to changes in recycling rate. For $\tau_r < \tau_c$, the deformation is governed by the buildup of elastic stress on network filaments, and effective viscosity becomes strongly dependent on recycling time.

These findings are in agreement with previous simulations of passive creep in cross-linked networks subjected to extensional stress [?] . Kim et al considered a different form of filament turnover (filament treadmilling) in networks with irreversible cross links. They identified two regimes of deformation depending on the level of applied stress and the filament turnover rate: a ?stress-dependent regime? in which filaments turnover before they are strained to an elastic limit and network deformation is linearly viscous and tuned by the turnover rate; and a ?stress-independent regime? in which filaments reach an elastic limit before turning over and the creep rate depends only on the turnover rate, and is insensitive to variation in applied stress. The short recycling time regime ($\tau_r < \tau_c$) that we observe, in which the mechanics are governed by filament extension, is directly equivalent to the stress-dependent regime described by Kim et al. For this regime, our model yields a theoretical description of the effective viscosity found in [?]. The $\tau_r > \tau_c$ regime that we observe here corresponds to the stress-independent regime of [?], but with a key difference. in [?], there was no cross-link unbinding so without of filament turnover, the network would not deform beyond its elastic limit. In contrast, our simulations always require non-zero cross-link slip so there is always some viscous network deformation. Therefore, in the

regime of long recycling times our model approaches the limit of cross-link dominated viscosity whereas the model of [?] approached an infinite viscosity limit.

4.1.2 *Filament recycling allows persistent stress buildup in active networks*

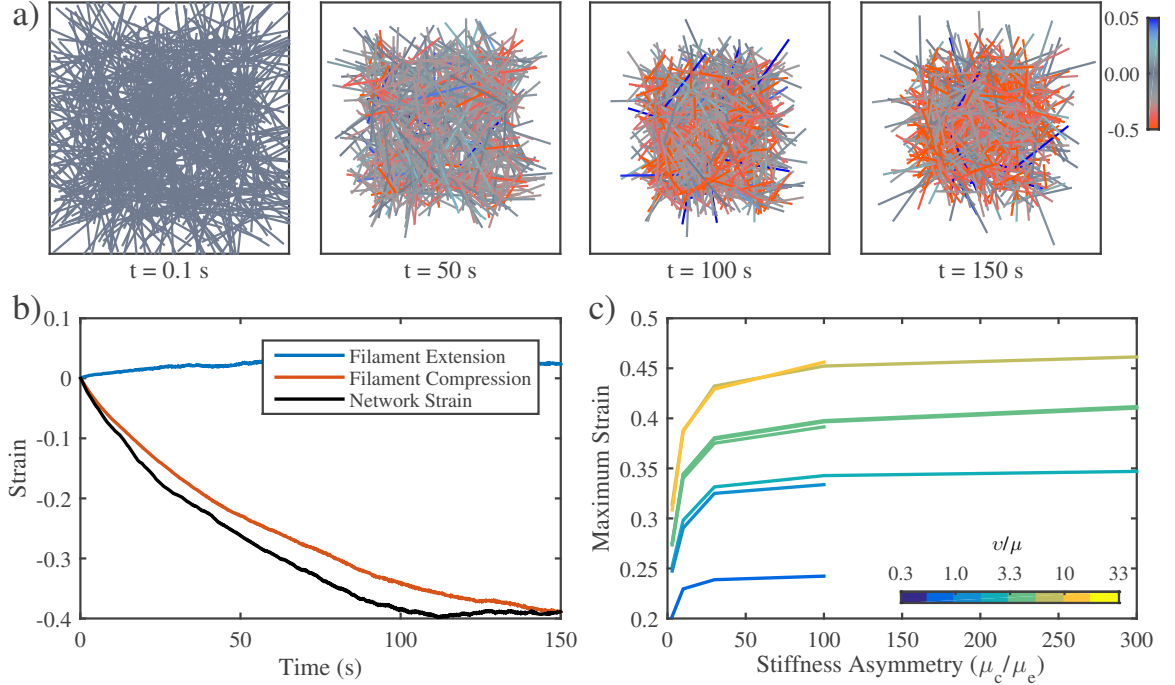


Figure 4.4: In the absence of filament recycling, active networks with free boundaries contract and then stall against passive resistance to network compression. **a)** Example of an active network contracting. Note the buildup of compressive stress as contraction approaches stall between 100 s and 150 s. Network parameters: $L = 5\mu m$, $l_c = 0.3\mu m$, $\xi = 100 nN \cdot s/\mu m$, $v = 0.1 nN$. **b)** Plots showing time evolution of total network strain and the average extensional (blue) or compressive (red) strain on individual filaments. **c)** The network's ability to deform relies on the magnitude of asymmetric filament compliance. Total network strain also increases with the applied myosin force v . Note that the extent of contraction approaches an asymptotic limit as the stiffness asymmetry approaches a ratio of ~ 100 .

In the absence of filament recycling, active networks with free boundaries contract and then stall against passive resistance to network compression.

Previous theoretical and experimental studies[?, ?, ?] identified asymmetric filament compliance and dispersion in motor force as minimal requirements for contraction of disordered networks. To test if our simple implementation of these two requirements (see Models section) was sufficient to produce macroscopic contraction, we simulated active networks that were unconstrained by external attachments. Turning on motor activity in an initially unstrained network at $t = 0$ produced a rapid initial contraction, followed by a progressive buildup of elastic stress due to compression of individual filaments and an \sim exponential approach to stall (Figure 4.4). The time to stall, τ_s , scaled as $L\xi/v$ (see Tearing of active networks is prevented via recycling. **a)** An active network undergoing large scale deformations due to active filament rearrangements. **b)** The same network as in a) but with a shorter filament recycling time. **c)** Time trace of internal stresses for network in panel a. **d)** Time trace of internal stresses for network in panel b), although the origins of this scaling relationship remain unclear. On a longer timescale, polarity sorting of individual filaments, as previously described [?, ?] rearranged the entire network, undoing the initial contraction (see S2 Video).

During the rapid initial contraction, bulk network strain matched closely the mean compressive strain on individual filaments Figure 4.4b, confirming that the origin of bulk contraction in our simulations is filament buckling due to asymmetric filament compliance, as predicted by [?, ?] and observed experimentally[?]. Contraction only occurred when the fractional motor activity $0 < \phi < 1$ (i.e. the fraction of filament intersections with active motors) was less than one, confirming the requirement for dispersion of motor activity (see Tearing of active networks is prevented via recycling. **a)** An active network undergoing large scale deformations due to active filament rearrangements. **b)** The same network as in a) but with a shorter filament recycling time. **c)** Time trace of internal stresses for network in panel a. **d)** Time trace of internal stresses for network in panel b). Thus, our model effectively captures a minimal mechanism for bulk contractility in disordered networks through asymmetric filament compliance and dispersion of motor activity.

We also determined how microscale parameters shape the rate and final extent of network contraction. Consistent with the idea that contraction stalls when the elastic

resistance to filament compression balances the contractile stress, the final extent of contraction increased sharply with motor activity (v) and with the asymmetry in filament stiffness (i.e. the ratio of the extensional and compressive stiffnesses μ_e/μ_c , Figure 4.4c,

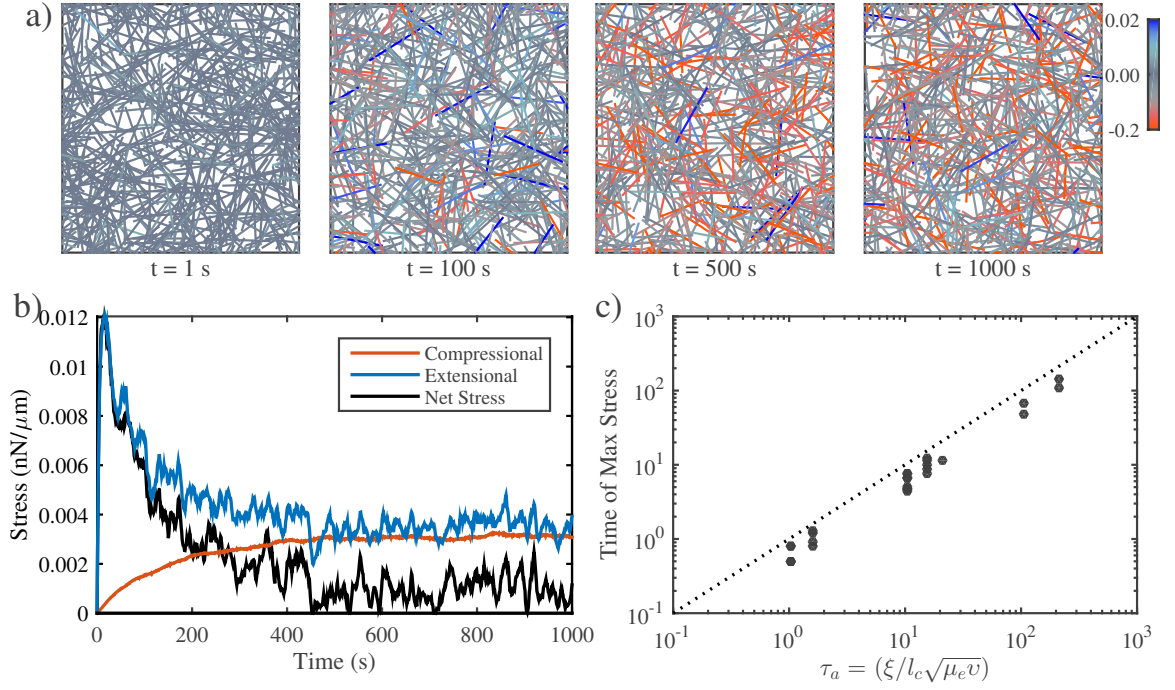


Figure 4.5: In the absence of filament recycling, active networks can only exert a transient force against a fixed boundary. **a)** Simulation of an active network with fixed boundaries illustrating progressive buildup of internal stress through local filament rearrangement and deformation. Note the progressive buildup of compressive stress on individual filaments. Network parameters: $L = 5 \mu m$, $l_c = 0.3 \mu m$, $\xi = 100 nN \cdot s/\mu m$, $v = 0.1 nN$. **b)** Plots of total network stress and the average extensional (blue) and compressive (red) stress on individual filaments for the simulation shown in (a). Rapid buildup of extensional stress allows the network transiently to exert force on its boundary, but this force is dissipated at longer times as internal extensional and compressive stresses become balanced. **c.** Measurement and prediction of the characteristic time (τ_a) at which the maximum stress is achieved.

Active networks can only exert a transient stress against a fixed boundary in the absence of filament recycling. The previous results reveal internal

limits on the contraction of networks with free boundaries. However networks typically build force and contract against an external resistance. Therefore, we also analyzed the buildup and maintenance of contractile stress in active networks contracting against a rigid boundary. We simulated active networks contracting from an initially unstressed state against a fixed boundary (Figure 4.5a), and monitored the time evolution of mean extensional (blue), compressional (red) and total (black) stress on network filaments (Figure 4.5b). We observed the same qualitative behavior for all network parameters examined: Total stress built rapidly to a peak value σ_a , and then decayed back to zero again. Sampling these dynamics over a large range of network parameters, we found that the peak stress occurred at a characteristic time, $\tau_a \sim \xi/l_c\sqrt{\mu_e v}$, as shown in Figure 4.5c. Although, the origins of this peculiar scaling are unclear, the measurement agrees with our intuitive predictions: The time to reach peak stress should vary directly with the cross-link coupling (ξ) and filament density ($2/l_c$), and it should inversely with the square root of both the filament stiffness (μ_e) and motor force (v).

The slower falloff of active stress involves two contributions: the first is slow dissipation of extensional stress on network filaments (blue curve in Figure 6B), reflecting a decrease in active stress generation. A similar effect was recently documented in detailed simulations of cross-linked actomyosin networks, where it was associated with large scale reorganization and collapse of network structure [?]. Here, we find that significant dissipation of extensional stress can also occur through more local rearrangements without loss of network structure (Figure 6A,B). The second contribution involves a gradual buildup of compressional stress (red curve in Figure 6B), that balances the active stress at steady state such the the total stress exerted on the network boundary falls to zero. This buildup of compressional stress occurs through purely local rearrangements in the absence of large scale deformation.

We were unable to find a simple dependencies on network parameters either dissipation of extensional stress or buildup of compressional stress. However, for all parameters we sampled, this timescale for decay of stress was significantly longer than the timescale for stress buildup, presumably because the initial buildup involves rapid loading of extensional stress on individual filaments, while the slower dissipation

requires local filament rearrangement.

Filament recycling allows networks to exert sustained stress on a fixed boundary. To explore how the fall-off in stress could be relieved by filament recycling, we again considered an active network contracting against a fixed boundary, using the same parameters as in Figure 4.5, but now we systematically varied filament recycling rates. Adding filament recycling produced two general effects: First, as in the passive case (Figure 4), filament recycling could prevent catastrophic tearing by continuously repairing local structural heterogeneities, and by steadily opposing the effects of local strain thinning (see S3 Fig). Second, we found that filament recycling resulted in biphasic modulation of the level of steady state stress.

For the same network parameters as in Figure 4.6a and slow filament recycling ($\tau_r = 1000s$), the network stress built rapidly, peaked, and then fell to a lower value that persisted for times much longer than τ_a . Up to a certain point, decreasing recycling time produced a monotonic increase in the steady state stress, although the steady state stress remained lower than its peak value. However, beyond this point, further decreases in recycling time lead to decreases in the steady state stress as well as sharp decreases in the peak stress. We reasoned that this bimodal dependence of steady state stress on recycling rates emerges from continuous replacement of strained with unstrained filaments, combined with the different timescales for buildup of extensional vs the slower dissipation of extensional stress and buildup of compressive stress (Figure 4.6b). If so, then lowering the recycling time τ_c should increase net stress until τ_c is approximately equal to τ_a , the time required to build peak stress from an initially unstressed state. For shorter recycling times, the average filament will not have time to build maximum extensional stress before turning over, and thus the steady state stress should decrease with further decreases in τ_c . Indeed, plotting normalized steady state stress (steady state stress/peak stress) vs normalized recycling time (τ_c / τ_a) confirmed that this biphasic dependence of steady state stress on recycling times holds for a large range of sampled values for network parameters 4.6d.

Similar to the passive response (i.e. Equation 4.3), we can approximate the dependence of the steady state stress on the filament recycling rate using a simple

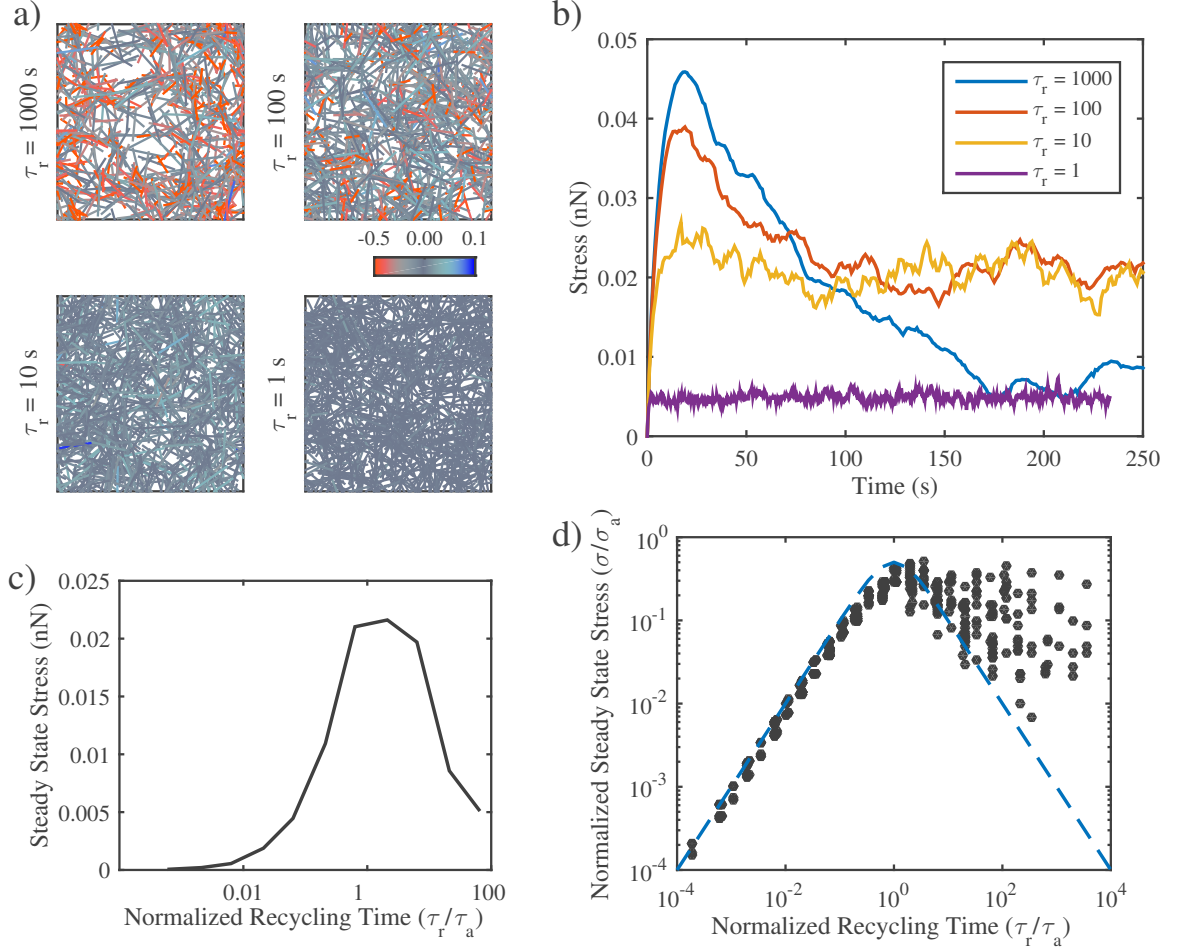


Figure 4.6: Filament recycling allows network to exert sustained stress on a fixed boundary. **a)** Snapshots from simulations of active networks with fixed boundaries for different timescales of filament recycling. Network parameters are the same as in Figure 6. Note that significant remodeling occurs for longer recycling times. **b)** Plots of net stress exerted by the network on its boundaries for different recycling times; for long-lived filaments, stress is built rapidly, but then dissipates. Increasing filament turnover rates reduces stress dissipation by recycling compressed filaments; however, very short recycling times prevent any stress from being built up in the first place. **c)** Plotting the steady state stress derived from the long term stress values of the stress in panel b. **d)** Normalized steady state stress as a function of normalized recycling time. The steady state stress is set by the timescale at which the network strain is refreshed relative to the timescale at which the max stress is reached. The values have been normalized to the predicted peak stress, σ_a in the absence of recycling. Blue dashed line indicates the approximation given in equation 4.4 for $n = 1$.

equation.

$$\sigma_{ss} = \frac{\sigma_{peak}}{(\tau_r/\tau_a)^n + \tau_a/\tau_r} \quad (4.4)$$

For $\tau_r \gg \tau_a$, this simplifies to $\sigma_{ss} \sim (\tau_a/\tau_r)^n$, while for $\tau_r \ll \tau_a$, this simplifies to $\sigma_{ss} \sim \tau_r/\tau_a$. What sets the scaling n remains unclear, and this scaling does not appear to be consistent across all simulation setups (Figure 4.6d). However, equation 4.4 still captures a qualitatively correct description of steady state stress in our simulation data.

4.1.3 Filament recycling tunes the balance between active stress buildup and viscous stress relaxation to generate flows

Thus far, we have considered independently how filament recycling tunes effective viscosity during passive deformation in response to an externally applied stress, and how filament recycling tunes the steady state stress produced by an active network against an external resistance. We next sought to characterize how filament recycling tunes the steady flows produced by gradients of motor activity as regions of high motor activity contract against the passive resistance of a neighboring region with low motor activity.

Filament recycling allows sustained flows in networks with non-isotropic activity. We imposed a continuously asymmetric distribution of motor activity on an initially uniformly dense network of passively cross-linked filaments by allowing a fraction of cross links to be active only in the right half of the simulation domain. Then we examined the time-dependent deformation of the network for a range of different filament recycling times Figure 4.7a. We observed a sharp dependence of steady flow on filament recycling rate Figure 4.7b,c. For very longer recycling times, ($\tau_r = 1000s$, dark blue line), there was a rapid initial deformation (contraction of the active domain and dilation of the passive domain), followed by a slow approach to a steady state flow characterized by slow contraction of the right half-domain and a matching dilation of the left half-domain (see Stress and strain profiles of networks

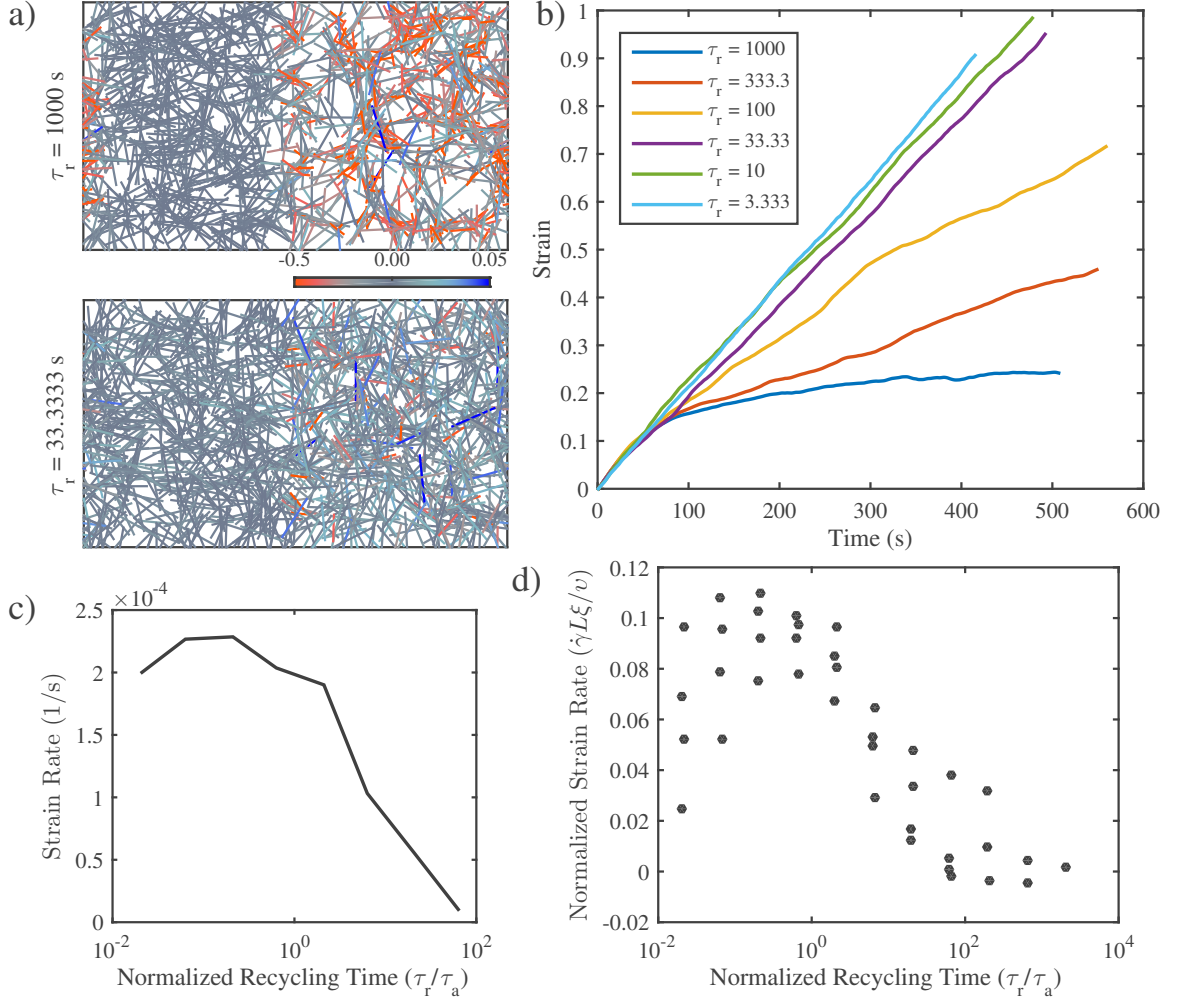


Figure 4.7: Filament recycling allows sustained flows in networks with non-isotropic activity. **a)** Example simulations of non-isotropic networks with long ($\tau_r = 1000$) and short ($\tau_r = 33$) recycling timescales. In these networks the left half of the network is passive while the right half is active. Network parameters are same as in Figures 4.5 and 4.6. Importantly, in all simulations $\tau_a < \tau_c$. **b)** Graph of strain for identical networks with varying recycling timescales. With long recycling times, the network stalls; reducing the recycling timescale allows the network to persist in its deformation. However, for the shortest recycling timescales, the steady state strain begins to slowly return to 0 net motion. **c)** Graph of network long-term strain rate as a function of recycling timescale for simulations in a) and b). **d)** Graph of network long-term strain rate as a function of recycling timescale across a wide range of parameter space. Note that networks only begin to maintain long-term flows when the recycling time is less than $100\tau_a$.

with contractile and passive domains. **a)** Blue line indicates strain velocity profile while orange represents net stress as measured in the main text. **b)** Same as panel a except for the condition where recycling time is 10 s. Note the increase in net stress and the corresponding increase in flow rate). However, with decreasing filament recycling times, we found the network was able to largely sustain its deformation and that the long term strain rate remained relatively high (Figure 4.7c). We repeated these measurements for more network parameters and found that at the shortest recycling timescales measured, we still saw the effective viscosity remaining relatively high, indicating that for short recycling times the effective viscosity may be somewhat buffered against variation in recycling times (Figure 4.7d).

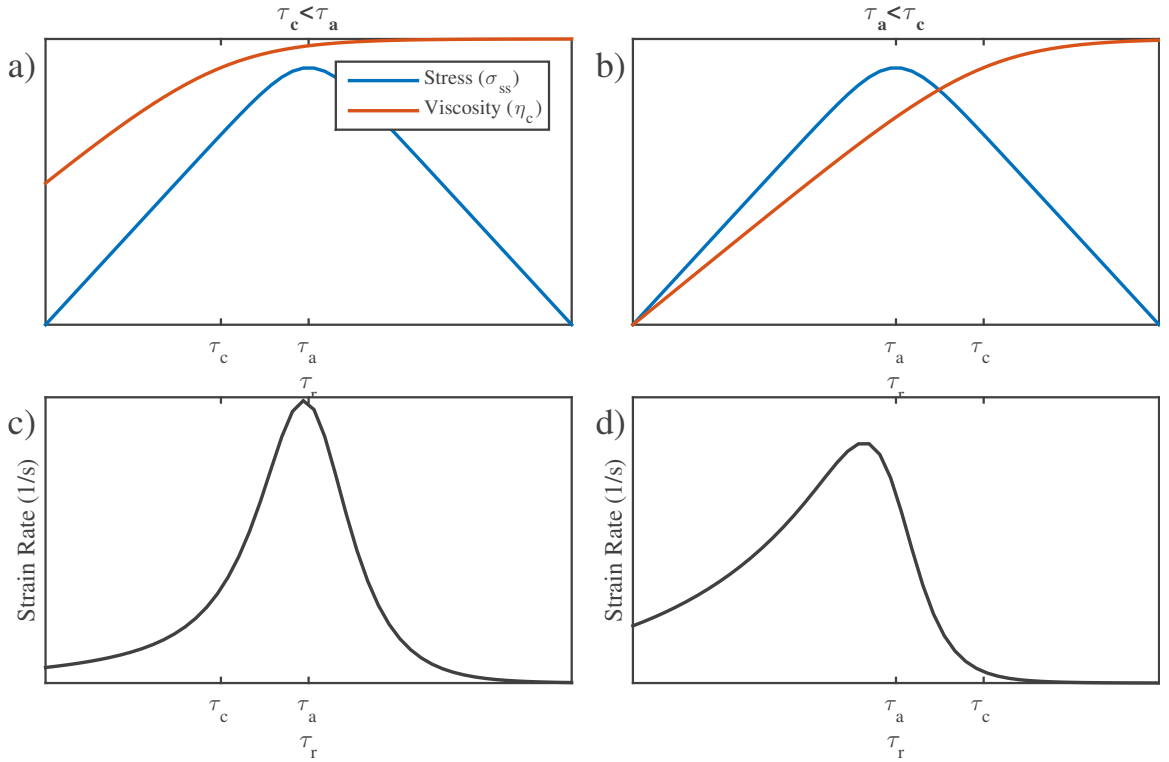


Figure 4.8: Filament recycling tunes the magnitudes of both effective viscosity and steady state stress. **a)** Dependence of steady state stress and effective viscosity on recycling time τ_r under the condition $\tau_c < \tau_a$. **b)** Same as a), but for the case where $\tau_a < \tau_c$. **c,d)** Resulting strain rates for network as a function of recycling time τ_r for the regimes in panels a and b..

Filament recycling tunes the magnitudes of both effective viscosity and steady state stress. This dependence of steady state deformation (flow) rate on filament recycling times can be understood in terms of our previous findings. During steady state flow, active contraction of the right half-domain is limited both by internal resistance to compression of filaments within the right half-domain (Figure 5), and by passive resistance of the left-half domain (Figure 4).

Monitoring these two forms of resistance as a function of filament recycling time for the simulations in Figure 8, we see that resistance to compression of filaments in the right half domain makes a significant contribution only for very low recycling rates. This is because using physiologically relevant values for network parameters (described above) sets up a condition where compressional resistance on filaments in the contracting right half domain takes longer to build than extensional resistance on filaments in the dilating right half-domain (i.e. $\tau_c < \tau_s$). As a consequence, except for very low recycling rates ($\tau_r > \tau_{crit}$), steady state deformation is governed by an equation of the form:

$$\dot{\gamma} = \frac{\sigma_{ss}}{\eta_r} \quad (4.5)$$

where σ_{ss} is the active stress generated by the right half-domain (less the internal resistance to filament compression), η_r is the effective viscosity of the left half domain and strain rate is measured in the left half-domain. Therefore, we can understand the dependence of network flow (i.e. strain rate) on filament recycling time τ_r in terms of the previously characterized dependencies of effective viscosity and steady state stress on τ_r (Figures 4.3d and 4.6d). In particular, recall that there is a transition in the dependence of η_r on τ_r at the characteristic time τ_c , and a transition in the dependence of σ on τ_r at the characteristic time τ_a . Thus, as shown in Figure 4.8, there are two qualitatively distinct cases for the dependence of strain rate on τ_r , depending on the relative magnitudes of τ_a and τ_c . For both cases, we expect a decrease in strain rate with filament recycling at long recycling times (where effective viscosity is insensitive to strain rate) and approach to a slowly varying strain rate at low recycling times, where both η_r and σ_{ss} fall off with different scalings. For $\tau_a < \tau_c$, we predict a

peak strain rate at intermediate recycling times followed by a rapid falloff at lower recycling times, whereas for $\tau_a > \tau_c$, we expect a more rapid approach to maximum strain rate and a slower fall off at lower recycling times. As shown in Figure 4.8d, for the range of network parameters we sampled, the strain rate rapidly increases as τ_r is lowered towards τ_a and then more slowly decays to 0 as τ_r is further decreased. This is to be expected because all the parameter values sampled (selected for physiological relevance) satisfied the condition $\tau_a > \tau_c$.

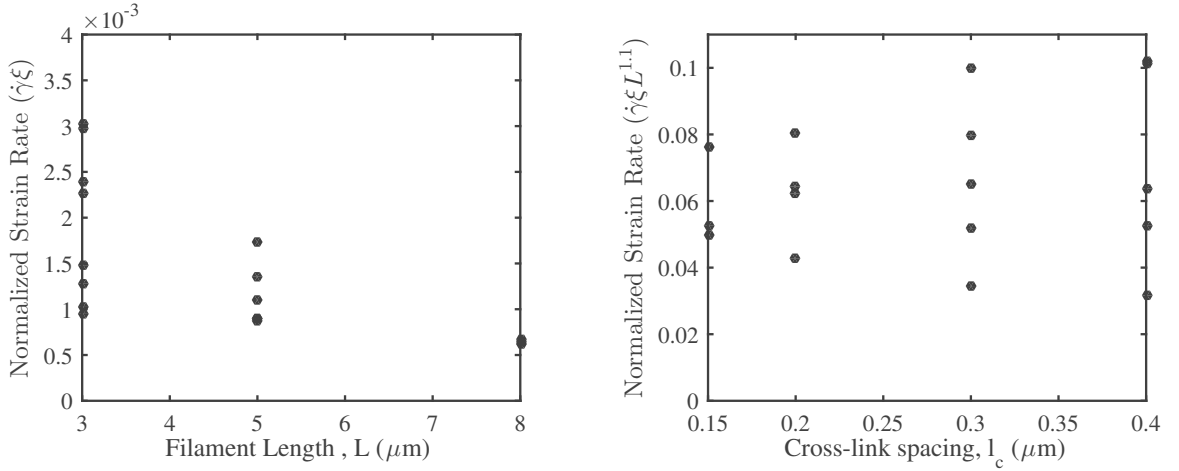


Figure 4.9: Filament recycling influences architectural control of flow rate. **a)** For a fixed filament recycling time, filament length tuned network deformation rate. **b)** Recycling rate is independent of cross-link spacing in this parameter space.

Filament recycling influences architectural control of flow rate. Finally, we examined how steady state flow depends on other network parameters when filament recycling rates are held constant. Interestingly, we found that flow rates are largely insensitive to cross link density (l_c) but vary inversely with filament length. Thus, in this region of parameter space, steady state flows may be buffered intrinsically against some forms of variation in network architecture.

4.2 Conclusion

Our work aimed to create a simulation framework that would allow us to analyze the origins of macroscopic flow in terms of a handful of physiologically relevant microscopic parameters. Toward this aim we developed a minimalist model of a 2D filament network and analyzed the network's reaction to a variety of situations. We found mathematical relationships that determined both the passive effective viscosity and the active stress generation of networks with and without recycling. From these relationships we were able to make predictions about the rates of network flow in non-isotropic networks mimicking those found in polarized eukaryotic actomyosin cortices.

Importantly, our work brings a theoretical understanding to the importance of actomyosin turnover in producing and maintaining long-term large scale flows. We propose the concept of "filament recycling" to refer to the multitude of biochemical interactions which can give rise to the piece by piece architectural resetting of filament networks. We believe that our analysis of networks in the presence of this filament recycling will be useful in further developing the qualitative and quantitative understanding the deformation of these complex networks.

4.3 Supporting Information

S1 Text. Bold the title sentence. Add descriptive text after the title of the item (optional).

S1 Fig. Bold the title sentence. Add descriptive text after the title of the item (optional).

S2 Fig. Mechanical properties of passive networks. **a)** Elastic modulus of networks. Our measurements closely match prediction of $G_0 \sim \mu/l_c$. **b)** Placeholder for inevitably another figure relevant to passive properties..

S3 Fig. Mechanical properties of active networks Add descriptive text after the title of the item (optional).

S4 Fig. Mechanical properties of active networks Add descriptive text after the title of the item (optional).

S6 Fig. Spatial velocity profile of networks containing passive and active domains.

S1 Table. Parameter values. List of parameter values used for each set of experiments.

S1 Video. Extensional strain in passive networks. Movie of simulation setup shown in Figure 4.1

S2 Video. Active networks contracting with free boundaries. Movie of simulation setup shown in Figure 4.4

Table 4.1: Simulation Parameter Values

Parameter	Figure 3	Figure 4	Figure 5	Figure 6	Figure 7	Figure 8
L	1, 3, 5, 7, 10	3	5	5	5	5
l_c	0.2, 0.3, 0.5, 0.8	0.3, 0.5	0.3	0.2, 0.3	0.2, 0.3	0.4
μ_e/μ_c	100	100	3 – 300	100	100	100
μ_c	0.01	0.01	0.01 – 0.3	0.01	0.01	0.01
ξ	10, 100	5, 10, 100	1, 10, 100	10, 100	10, 100, 330	10, 100
v			0.1, 0.3, 1	0.1, 1	0.1, 1, 3	0.1, 1
ϕ			0.25	0.5	0.25, 0.75	0.25
τ_r		0.1 – 10^4			0.01 – 10^3	0.01 – 10^3
σ	0.0002 – 0.01	0.00003 – 0.005				

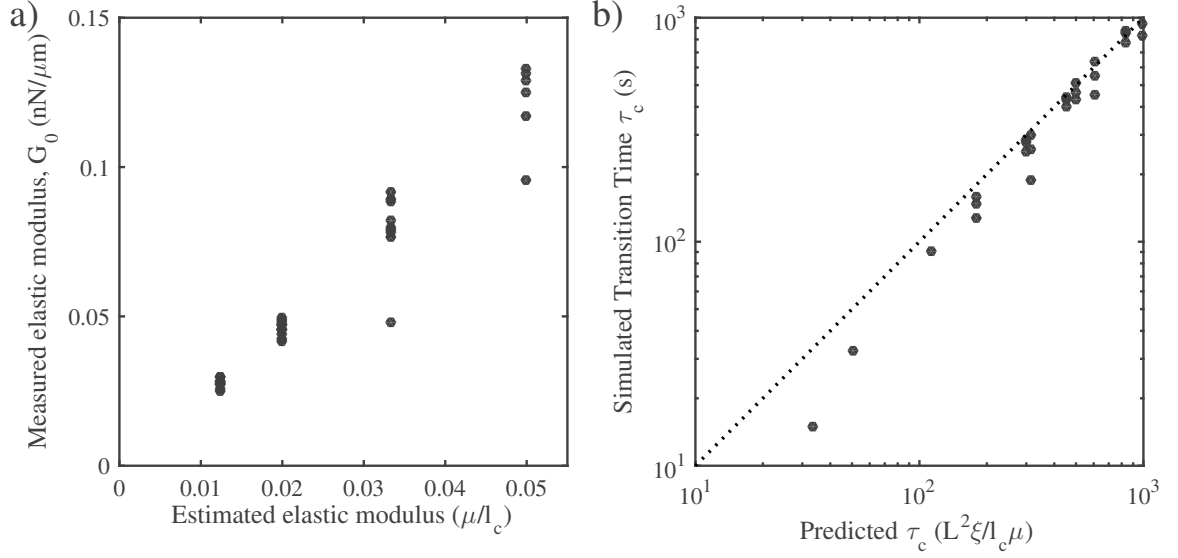


Figure 4.10: Mechanical properties of passive networks. **a)** Elastic modulus of networks. Our measurements closely match prediction of $G_0 \sim \mu/l_c$. **b)** Placeholder for inevitably another figure relevant to passive properties.

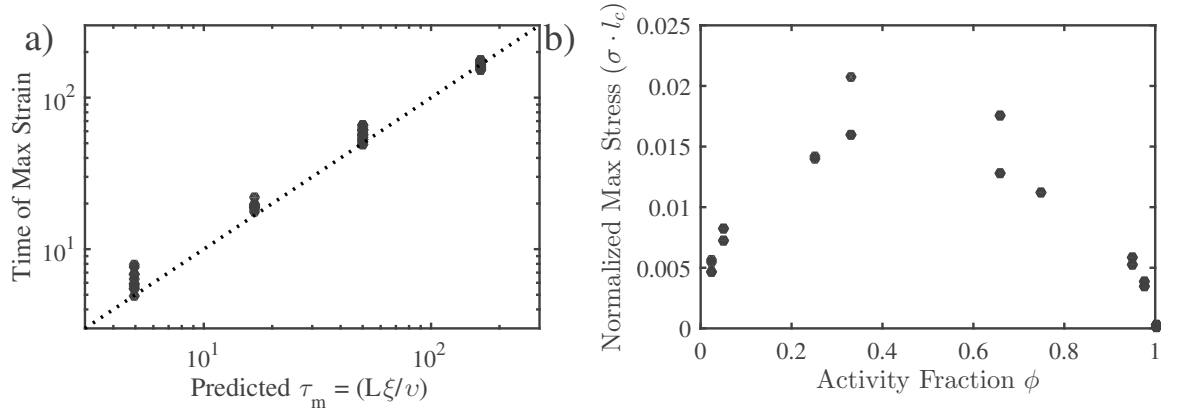


Figure 4.11: Mechanical properties of active networks. **a)** Timescale of maximum strain in networks free to contract. This relationship was found phenomenologically. **b)** Dependence of network stress on the fraction of cross-links which are active. Note that the network stress approaches 0 as ϕ approaches 0 or 1.

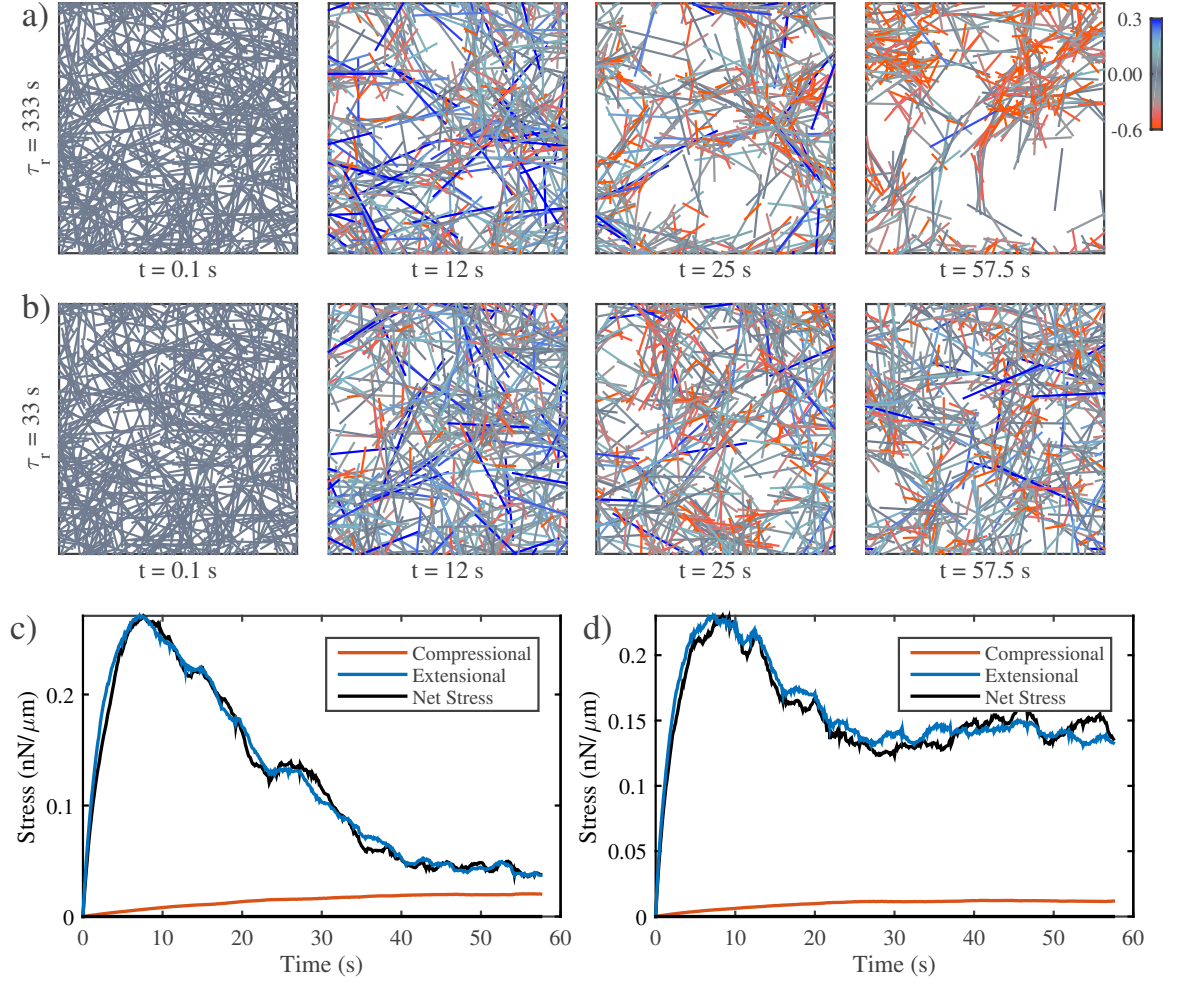


Figure 4.12: Tearing of active networks is prevented via recycling. **a)** An active network undergoing large scale deformations due to active filament rearrangements. **b)** The same network as in a) but with a shorter filament recycling time. **c)** Time trace of internal stresses for network in panel a. **d)** Time trace of internal stresses for network in panel b.

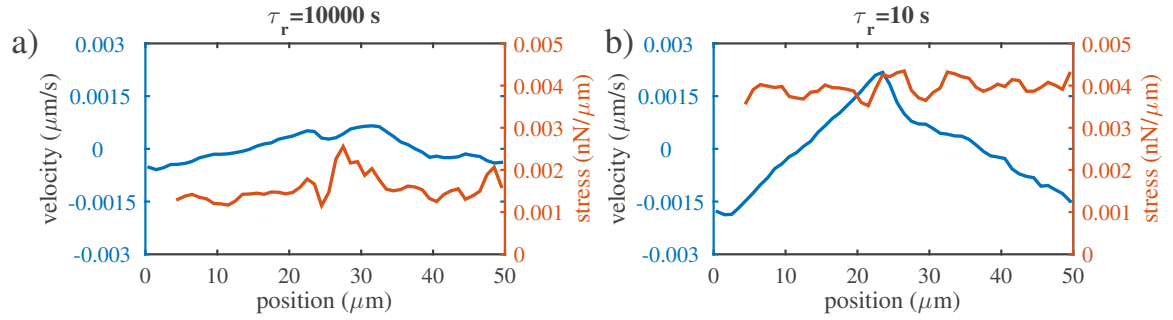


Figure 4.13: Stress and strain profiles of networks with contractile and passive domains. **a)** Blue line indicates strain velocity profile while orange represents net stress as measured in the main text. **b)** Same as panel a except for the condition where recycling time is 10 s. Note the increase in net stress and the corresponding increase in flow rate.

CHAPTER 5
A MODEL OF UPSTREAM ACTOMYOSIN
REGULATORS IN PULSED CONTRACTIONS

CHAPTER 6

PHASES OF DEFORMATION IN FILAMENT NETWORKS WITH CROSS-LINK SLIP

6.1 Results

6.1.1 Steady-state Approximation of Effective Viscosity

We begin with a calculation of a strain rate estimate of the effective viscosity for a network described by our model in the limit of highly rigid filaments. We carry this out by assuming we have applied a constant stress along a transect of the network. With moderate stresses, we assume the network reaches a steady state affine creep. In this situation, we would find that the stress in the network exactly balances the sum of the drag-like forces from cross-link slip. So for any transect of length D , we have a force balance equation.

$$\sigma = \frac{1}{D} \sum_{\text{filaments}} \sum_{\text{crosslinks}} \xi \cdot (\mathbf{v}_i(\mathbf{x}) - \mathbf{v}_j(\mathbf{x})) \quad (6.1)$$

where $\mathbf{v}_i(\mathbf{x}) - \mathbf{v}_j(\mathbf{x})$ is the difference between the velocity of a filament, i , and the velocity of the filament, j , to which it is attached at the cross-link location, \mathbf{x} . We can convert the sum over cross-links to an integral over the length using the average density of cross-links, $1/l_c$ and invoking the assumption of (linear order) affine strain rate, $\mathbf{v}_i(\mathbf{x}) - \mathbf{v}_j(\mathbf{x}) = \dot{\gamma}x$. This results in

$$\begin{aligned} \sigma &= \frac{1}{D} \sum_{\text{filaments}} \int_0^L \xi \cdot (\mathbf{v}_i(\mathbf{s}) - \mathbf{v}_j(\mathbf{s})) \frac{ds \cos \theta}{l_c} \\ &= \sum_{\text{filaments}} \frac{\xi \dot{\gamma} L}{l_c} \cos \theta \cdot \left(x_l + \frac{L}{2} \cos \theta \right) \quad (6.2) \end{aligned}$$

Here we have introduced the variables x_l , and θ to describe the leftmost endpoint and the angular orientation of a given filament respectively. Next, to perform the sum over all filaments we convert this to an integral over all orientations and endpoints that intersect our line of stress. We assume for simplicity that filament stretch and filament alignment are negligible in this low strain approximation. Therefore, the max distance for the leftmost endpoint is the length of a filament, L , and the maximum angle as a function of endpoint is $\arccos(x_l/L)$. The linear density of endpoints is the constant $D/l_c L$ so our integrals can be rewritten as this density over x_l and θ between our maximum and minimum allowed bounds.

$$\sigma = \frac{1}{D} \int_0^L dx_l \int_{-\arccos(x_l/L)}^{\arccos(x_l/L)} \frac{d\theta}{\pi} \frac{\xi \dot{\gamma} L}{l_c} \cdot \frac{D}{L l_c} \cdot (x_l \cos \theta + \frac{L}{2} \cos^2 \theta) \quad (6.3)$$

Carrying out the integrals and correcting for dangling filament ends leaves us with a relation between stress and strain rate.

$$\sigma = \frac{(L - 2l_c)^2 \xi}{4\pi l_c^2} \dot{\gamma} \quad (6.4)$$

We recognize the constant of proportionality between stress and strain rate as a viscosity. Therefore, our approximation for the effective viscosity, η_{eff} , at steady state creep in this low strain limit is

$$\eta_{eff} = \frac{(L - 2l_c)^2 \xi}{4\pi l_c^2}. \quad (6.5)$$

As illustrated in Figure 6.1, under moderate strains ($\gamma < 0.2$), our simulations show that in the high density limit, our theoretical approximation from Eqn 6.5 is highly accurate at explaining the network behavior. Aside from a geometrical factor, our approximation is valid for both shear and extensional stresses applied to the network.

As the density of the network approaches the breakdown limit, the effective viscosity diverges from our expected value. At the low connectivities, our expected viscosity goes to 0, but the medium viscosity begins to take over as we cross the percolation threshold at $L/l_c \sim 6$.

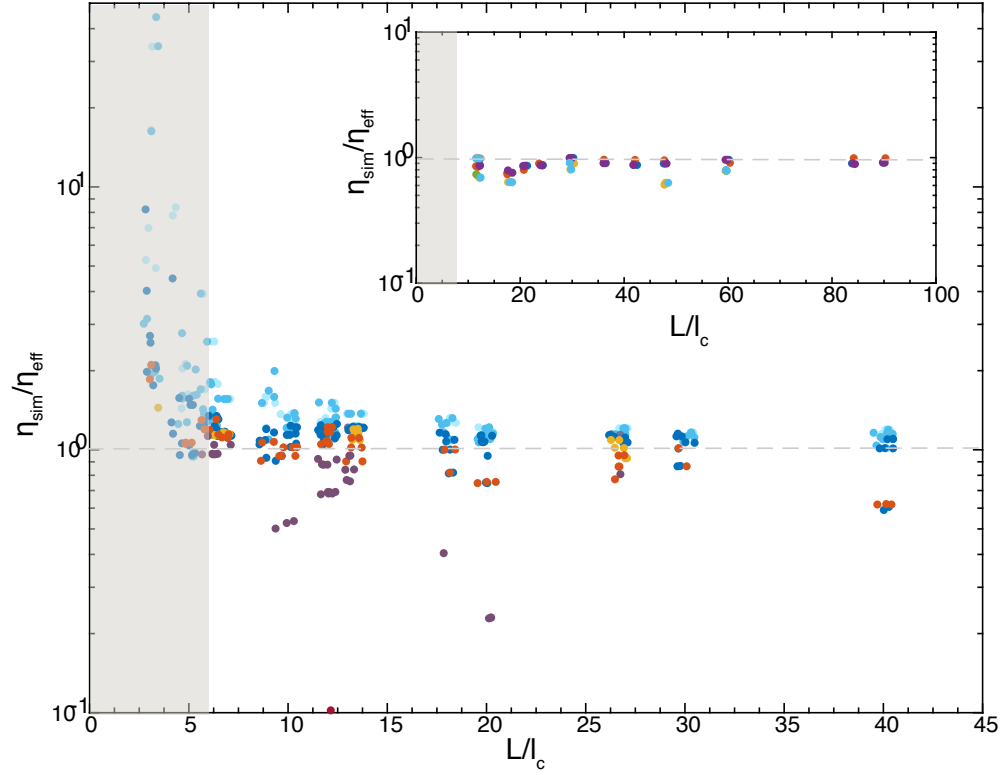


Figure 6.1: Ratio of effective viscosity measured by shear simulation to predicted effective viscosity as a function of connectivity, L/l_c . Inset: Same measurement for extensional simulations

In addition to changing the architecture and effective drag coefficient, we also validated the generality of our approximation by varying simulation size, medium viscosity, filament stiffness, and applied stress. We were able to find a slight trend that depended on filament stiffness as indicated in the difference between blue and red data points in Figure 6.1. The deviation from our approximation and variability in results manifested itself more strongly when filaments were highly compliant. To investigate this effect further, we next performed a more detailed analysis of the creep response while varying filament compliances.

6.1.2 Effects of Filament Compliance

The effect of filament compliance on cross-linked networks under strain is a subject of active research at the moment [Sayantan]. Therefore, we wished to use our computational approach to extend our understanding of filament networks in the regime of non-negligible filament compliance.

In irreversibly cross-linked polymer networks, filament compliance is known to give rise to elastic deformation of the network as described in[?, ?].

During the initial affine deformation immediately after the application of an external stress, we see a rapid stretch of filaments, $\langle \delta L/L \rangle_0$, in response to the affine purely mechanical strain, γ_{xy} , which closely follows $\langle \delta L/L \rangle_0 = \gamma_{xy} \sin(\theta) \cos(\theta)$. As shown in Figure 6.2, during the first phase in our simulations, the total network strain (solid) is described almost entirely by the strain of the filaments (dotted).

However, in the presence of cross-link slip, the filaments are not permanently constrained to remain at $\langle \delta L/L \rangle_0$. Interestingly, although the mean filament strain stays approximately constant, the distribution of individual filament strains broadens around the affine approximation as shown in the inset of Figure 6.2.

During the period where crosslink slip allows changes in the filament length distribution, we also find a long-lived intermediate relaxation phase that deviates from both the initial purely elastic relaxation and the later purely viscous behavior of section 6.1.1. In Panel B of Figure 6.2, we show that the standard deviation of the filament stretch distribution continues to increase throughout the period that the strain rate is non constant.

Approximating this broadening as a normally distributed variation in filament stretched length throughout the network (\mathcal{N}) with a time varying standard deviation, $\sigma(t)$, we have $\delta L/L = \langle \delta L/L \rangle_0 + \sigma(t) \cdot \mathcal{N}$. This has an effect on the total mechanical energy stored in the network $\mathcal{H} \sim \langle \delta L/L \rangle^2 = \langle \delta L/L \rangle_0^2 + \sigma(t)^2$. Therefore, the network will deform further while some strain energy is being stored in the further stretching filaments.

Eventually the contribution from slow filament stretching will become negligible compared to that from pure cross-link slip on rigid rods. This occurs on a timescale

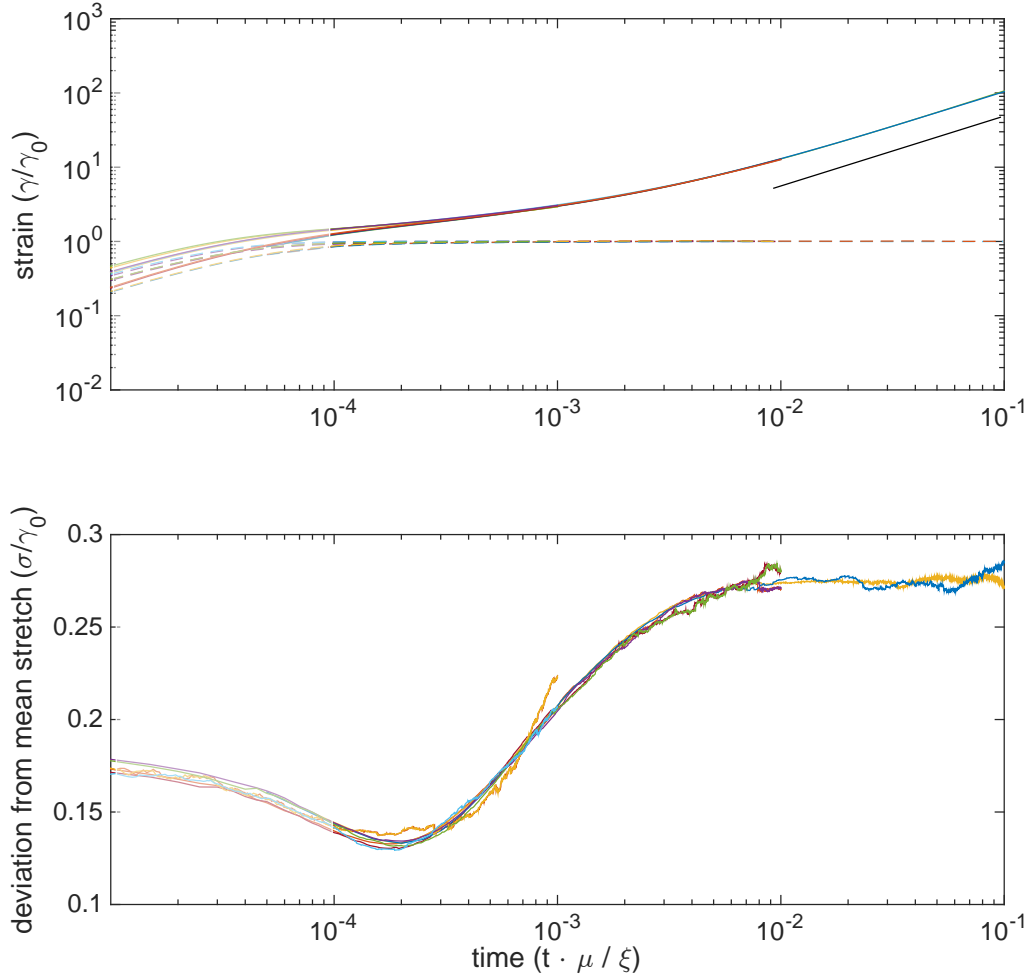


Figure 6.2: Network and filament strain for different filament drag coefficient parameters. (top) Plot of total strain normalized by the final mean filament strain, $\delta L/L$. Dashed lines show the amount of strain from affine mechanical stretching. (bottom) Standard deviation of filament extension for the networks in A. Note that the creep compliance in A becomes constant (slope 1) only after the spread in filament extension in B stops increasing. Colors indicate unique experimental conditions.

similar to that of cross-link slip and causes the effective viscosity to decay back toward the rigid limit. This gives rise to a less-than-linear creep response during times after the initial elastic relaxation but before full filament relaxation from cross-link slip. As shown in Figure 6.3, the transition begins to take place as network strain reaches

10 to 100 times the strain from pure mechanical stretching, $\gamma_0 = \delta L/L$, and this property is independent of the magnitude of the rate of strain.

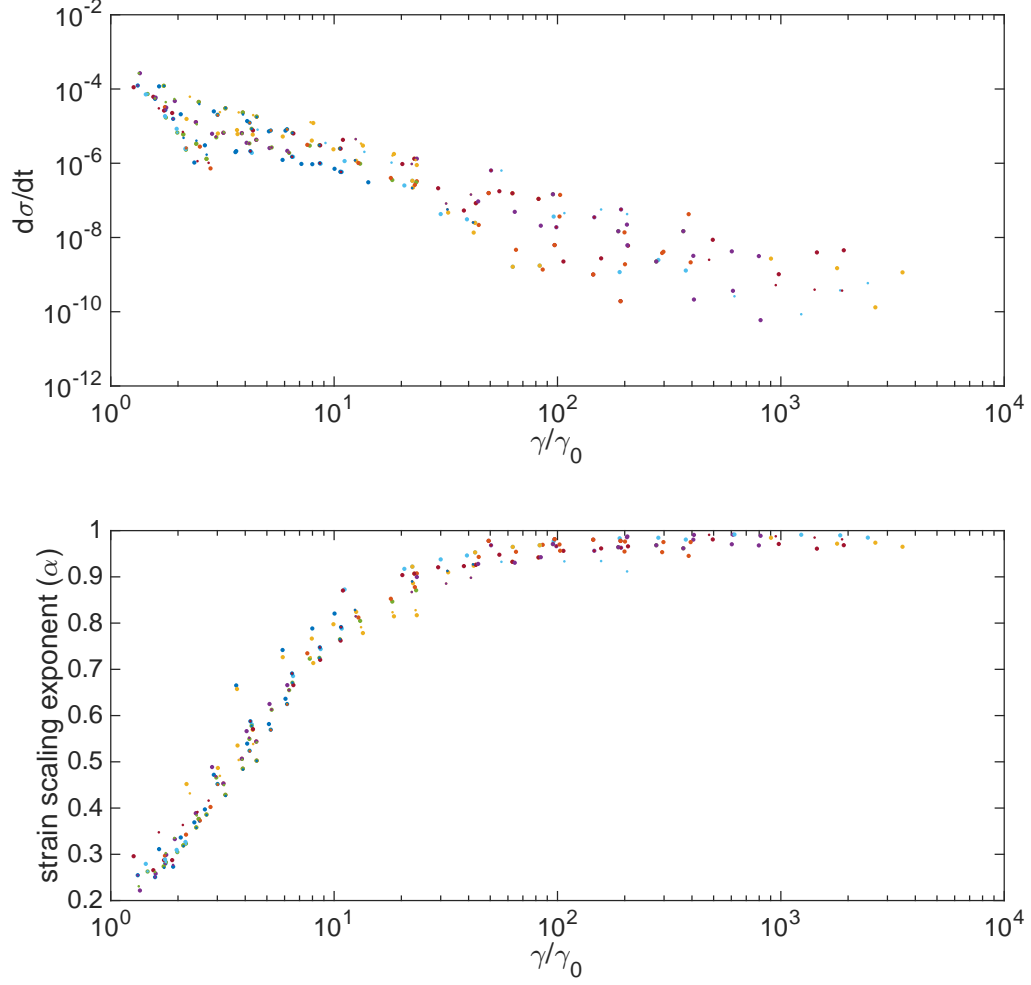


Figure 6.3: Sublinear network strain ends as change in filament strain decays. (top) Change in standard deviation of filament strain, σ , as a function of strain relative to pure mechanical strain. (bottom) Dependence of strain rate exponent as a function of strain relative to pure mechanical strain, γ_0 . Colors indicate unique experimental conditions.

6.1.3 *Alignment at High Strain and Network Tearing*

Once the network is able to accumulate a large strain, the assumption of nearly uniform distributions of filament orientations begins to break down.

At this point the filament orientations become unevenly distributed $\langle \delta L/L \rangle \neq \gamma_{xy} \sin(\theta) \cos(\theta)$, with a larger number of filaments aligning in the direction of extension rather than compression. Filament alignment, conceptually, causes the formation of subdomains that no longer span the space of the network. To the authors' knowledge an exact derivation of the dependence of network connectedness on filament alignment has not been carried out, but Monte Carlo simulations have been used to show that alignment does indeed lead to lower connectedness[?].

We find that over time, the orientational distribution of the filaments begins to peak around 45 degrees as the large strain induces alignment. In Figure 6.4, we see that as the angular standard deviation falls, this reorientation eventually leads to fewer bonds bridging the network perpendicular to the line of strain. As this connectivity begins to noticeably decrease, the observed effective viscosity decreases as well, giving rise to greater than linear creep. From the inset of Figure 6.4 we can also see that the onset of phase D occurred before the network had completely reached phase C, leading to a rapid transition between sub-linear and super-linear creep. Finally, it should be noted that the end of this simulation resulted in the network tearing apart.

6.1.4 *Phase Diagram of Dominant Behavior*

In Figure 6.5, we illustrate the four stereotyped phases of the general mechanical behavior that we observed in our networks. A deforming network typically undergoes a rapid filament stretching, a slower relaxation of elastic constraints, a phase of purely viscous cross-link slippage, and an eventual alignment and breakdown of network connectivity.

Finally, to explore the transitions between the various phases, we measured the creep response for a computationally tractable network ($L/l_c = 25$), as we varied the filament extensional modulus, μ , and the cross-link friction coefficient, ξ . In Figure

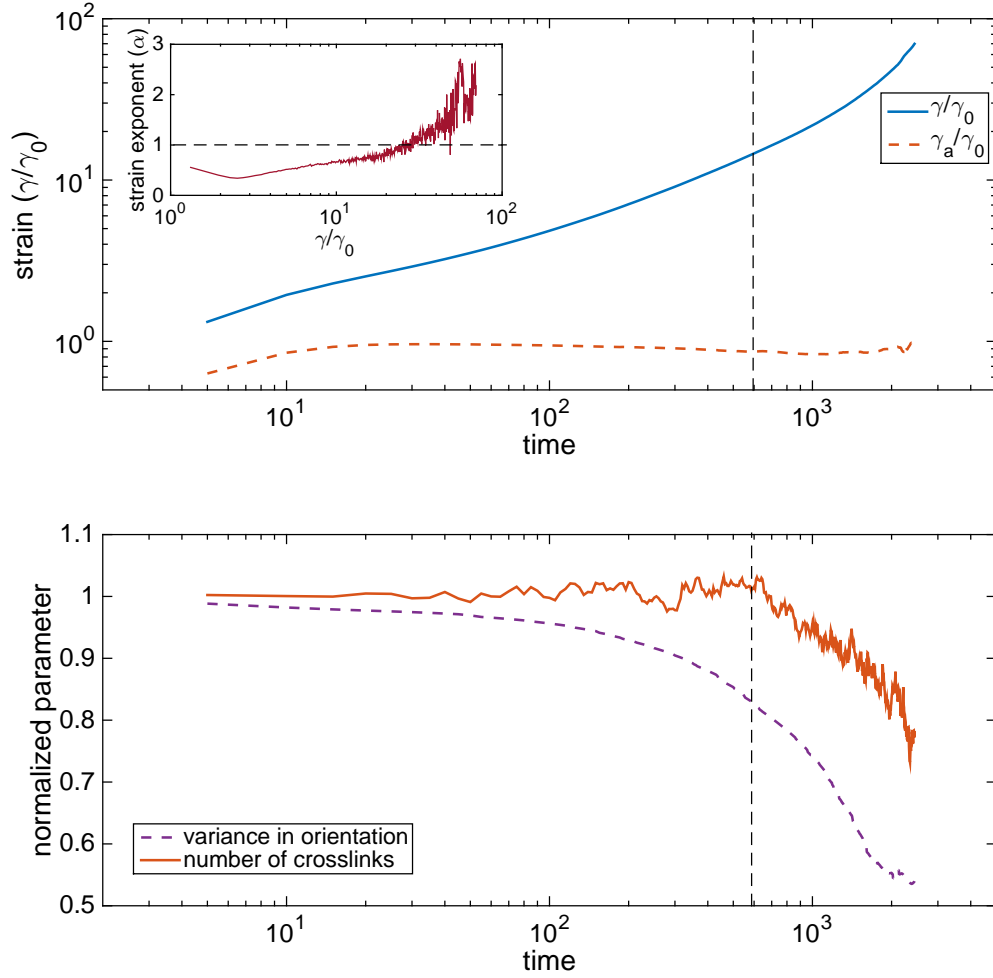


Figure 6.4: Creep response of a network transitioning to phase D. (top) Strain curves for a network undergoing large scale deformation. Inset shows strain exponent as a function of strain (exponent passes 1). (bottom) Traces for the variance in filament orientation and number of cross links. Vertical dashed line shows the point where the strain exponent becomes greater than one.

6.6, we classified parameter sets based on their strain exponent. We can see the trends for the transitions between phases A, B, and C. The line for the transition to D is still speculative at this time.

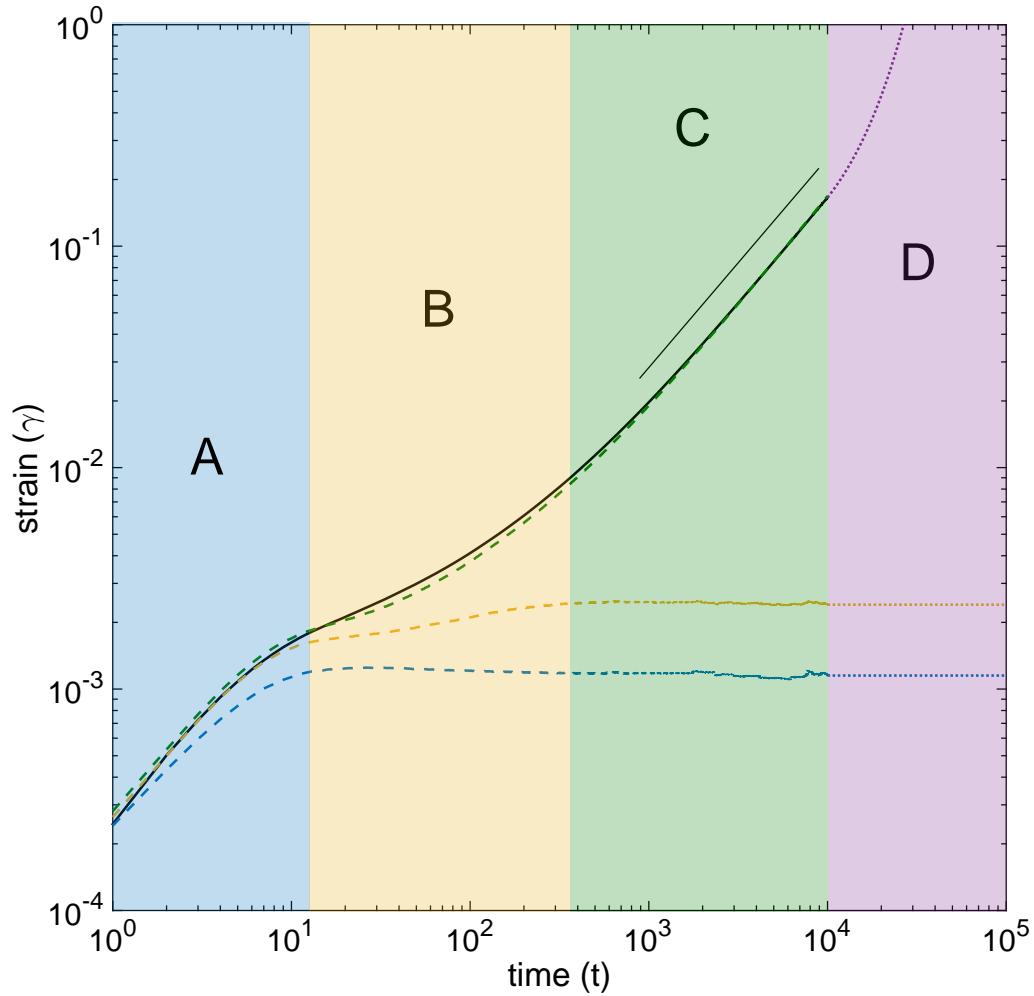


Figure 6.5: Schematic of the general creep response of compliant filament networks illustrating the 4 phases of deformation: A) rapid mechanical response, B) combination of slow filament stretching and cross-link slip, C) cross-link slip dominated (line indicates slope of one), D) network tearing from filament alignment. Note that the portion of the curve in section D is only a hypothetical continuation of the actual data.

6.1.5 Frequency dependent modulus

This section will include a figure on the frequency dependent modulus once I get those.

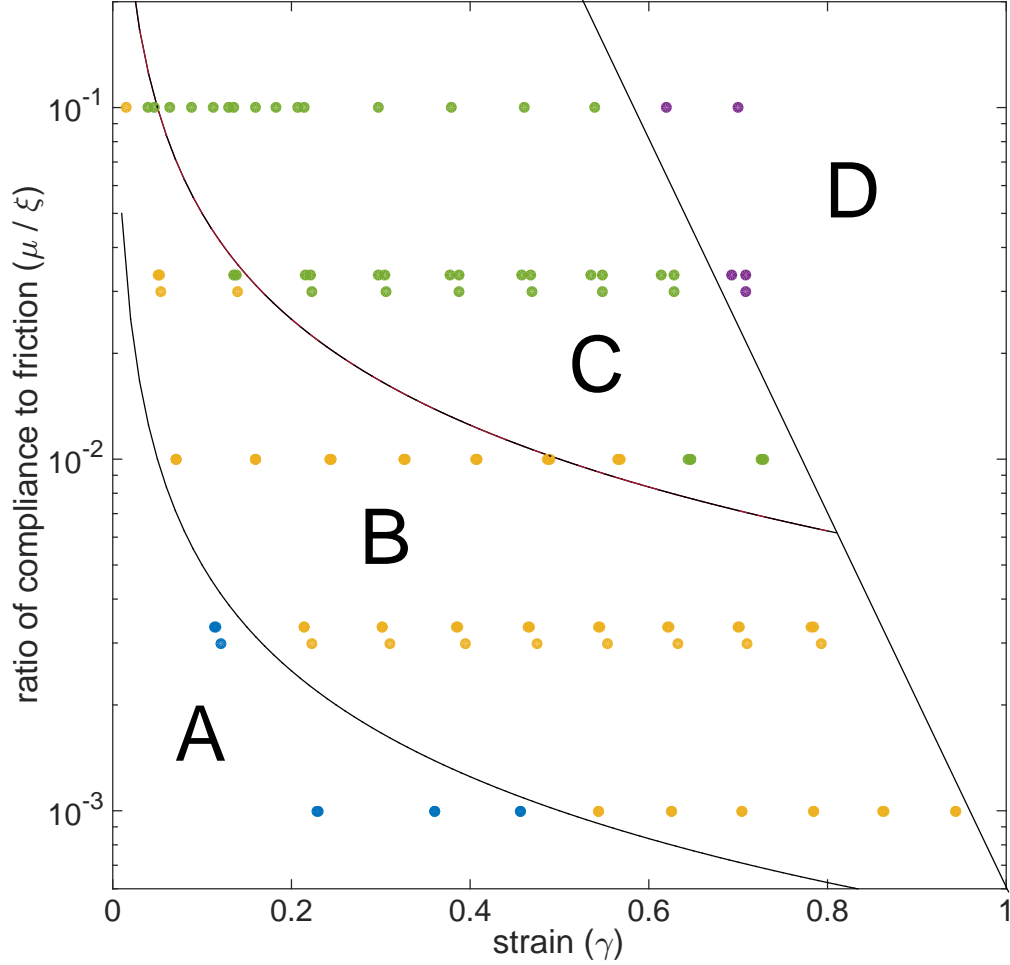


Figure 6.6: phase diagram of creep response for different filament extension, μ and cross-link friction, ξ . Yellow, green, and purple dots correspond to creep measurements $\gamma \sim t^\alpha$ with $\alpha < 0.92$, $0.92 < \alpha < 0.98$, or $\alpha > 0.98$ respectively. Blue dots represent creep measurements where $\gamma_{total} < 2\gamma_{mechanical}$

6.1.6 Strain Memory

Finally, we found an interesting behavior when we introduced non-linear extensional stiffness into our filaments. When the network is allowed to relax to its unstrained state, there is generally a time comparable to the period of strain storage over which the energy in the network is relaxed away.

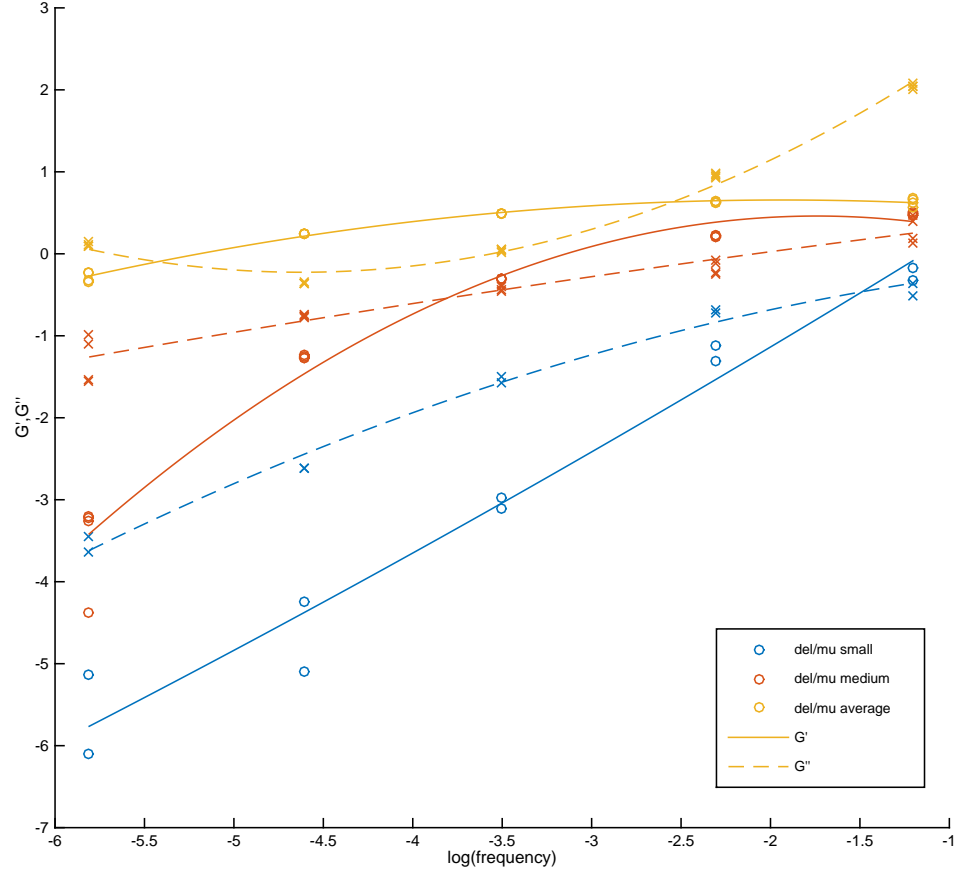


Figure 6.7: Frequency dependent moduli for networks.

We observed deviations from this behavior by applying stepwise stress pulses to simulated networks, and observing whether the network behaves identically upon reversal of the applied stress direction. If the network has no strain memory then each reversal will result in an identically shaped creep curve. However, when we include nonlinear filament extension in our model, we find that the mechanical strain can be stored for longer periods of time than it took to entrain the network.

This behavior mimics recent experiments in filamin cross-linked networks. Filamin provides a high level of compliance to a network ($\gamma_0 > 0.5$) without substantial cross-link unbinding. This allows large scale rearrangements to take place without driving

very much cross-link slip, similar to the conditions in section 6.1.2. However, if we force individual filaments to undergo a strongly nonlinear stiffening at strains above 5%, we find an interesting long term "strain storage."

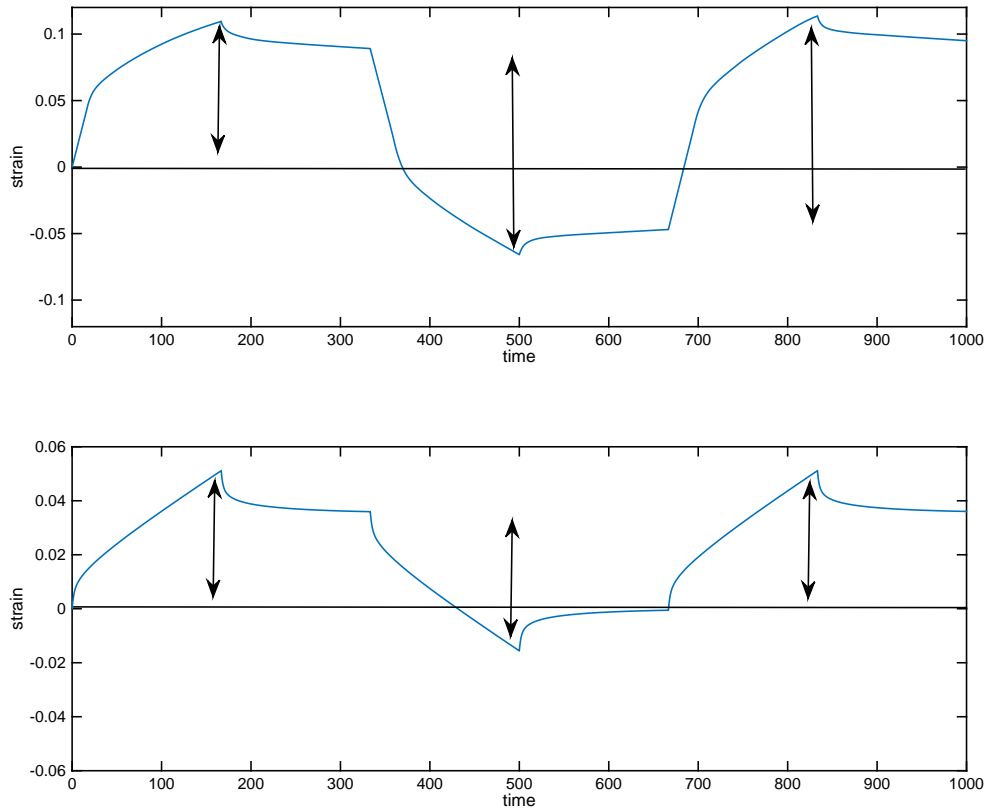


Figure 6.8: Creep curves in the presence of reversing applied stress for (a) nonlinear extension or (b) linear extension. Note that for linear filaments the induced strain returns to approximately 0 after a complete cycle, while in the nonlinear case the cycle is not completely reversible.

Figure 6.8 shows that the strain storage occurs, but I will need time for further study to build the full analytical picture of where when and why this happens in my model.

6.2 Summary and Conclusions

We have proposed a simplified effective friction model for understanding 2D cross-linked networks. Our model extends previous Mikado and lattice models to include effects of cross-link relaxation. We expect that our model can confer insights into mechanisms of network stress relaxation in quasi-2D networks such as those found in *in vitro* actin monolayer experiments[?] as well as in eukaryotic actomyosin cortices[?].

Our model is the first to address the plausible dependence of network effective viscosity on network structural properties. This led to a derivation of an estimate for the long timescale creep rate of networks under constant stress. Although this derivation neglects possible frequency dependence at short timescales, this finding offers a potential framework for addressing the dependence of network deformation rate on filament concentration and length.

Additionally, our simulations suggest that, in the presence of constant shear stress, cross-link friction will also produce a long-lived phase of sublinear creep as filaments relax from their affine stretched position. While this phase may transiently resemble more explicit 3D models such as [?], it is clear that our model differs by predicting that network will achieve a constant effective viscosity more rapidly. In particular, we predict that this relaxation will occur at a rate similar to that of rate of cross-link slip derived strain and will therefore be negligible after the network has slipped by roughly ten times the magnitude of the purely affine mechanical deformation.

In building our model we have neglected any other sources of potential mechanical relaxation in order to simplify our analysis. In the future, we hope to extend our model to include biochemically driven forms of relaxation such as filament turnover or regulated cross-link unbinding.

This model forms a basis for addressing 2D filament network deformation, and it proposes a simplified formulation of important qualitative properties. In this way we are able to address potentially general phases of network deformation and delineate what network properties may give rise to them. This may provide an important starting point for addressing the general importance of network structure in more complex networks containing active elements.

6.3 Network Tearing under Extensional Stress

6.3.1 Extensional Thinning and Network Tearing

For moderate extensional stresses, the rigid filament approximation of the effective viscosity simply picks up a different geometrical factor out front.

However, at higher stress and in the presence of different things happen.

$$\frac{\partial l_c}{\partial t} = l_c \dot{\gamma} = \frac{l_c \sigma}{\eta} \sim l_c^3 \frac{\sigma}{L^2 \xi} \quad (6.6)$$

We can see that the rate of network thinning accelerates as we would expect. When the network reaches some minimum connectivity we assume that it stops behaving as a continuum material and the network tears irreversibly.

$$\tau_{break} = \frac{\eta_{eff}}{2\sigma} \cdot \left(1 - \frac{l_c^2}{l_{break}^2}\right) \quad (6.7)$$

This provides us with an estimate of the timescale of catastrophic breakdown for a network with a given initial architecture and molecular drag.

6.3.2 Tearing Events During Extensional Strain

This behavior is caused primarily by the low density network undergoing tearing events that interrupt global connectedness.

6.4 Deriving Molecular Drag Coefficients

Thus far, the idea of a molecular drag coefficient was taken as a phenomenological, measured parameter for a given experimental setup. While this is a sufficient pragmatic justification, it's useful to try to motivate the quantitative value of this drag coefficient by connecting it to the underlying cross-link properties of binding affinity, concentration, and extensibility.

To do this we'll imagine the simplified case of two cross linkers sliding past each other in one dimension. In this case, assume that we have an equilibrium number

of bound cross-linkers, n_B , each of which is displaced from its equilibrium length by some distance x . Each cross linker unbinds with rate k_{off} and rebinds at it's relaxed position ($x = 0$) with rate k_{on} . At the same time, all the cross linkers are being pulled from their relaxed position at a rate, v , which is simply the rate at which the filaments are sliding past each other.

We can write the differential equation for the change in the density of cross-links, ρ , at displacement x as they are pulled upon, bind, and unbind.

$$\frac{\partial \rho}{\partial t} = -k_{off}\rho(x) - v\frac{\partial \rho}{\partial x} + k_{on}\delta(x) \quad (6.8)$$

Recognizing that $\int \rho(x) dx = n_B$ implies $k_{on} = k_{off}n_B$, we can find the steady state solution

$$\rho(x) = \frac{n_B k_{off}}{v} \cdot \exp\left(-\frac{k_{off}}{v}x\right) \quad (6.9)$$

If each cross-link has a spring constant μ_c , then we can equate the force on all cross-links to the applied force that is sliding the filaments past each other. Realistically, the spring constant and binding affinity would be functions of the cross-link stretch, but here we are taking them as approximately constant.

$$\int_0^\infty \rho(x) \mu_c x dx = v \frac{\mu_c n_B}{k_{off}} = F_{app} \quad (6.10)$$

a

Therefore, the term next to v , (i.e. $\frac{\mu_c n_B}{k_{off}}$) would be equal to our molecular drag coefficient, ξ . Assuming approximately 1 cross link per filament overlap, and using parameter estimates culled from Ferrer et al., we build the following table of estimates for ξ .

cross-linker type	α -actinin	filamin-A
dissociation constant (s^{-1})	0.4	0.6
spring constant ($nN/\mu m$)	455	820
drag coefficient, ξ ($\frac{nN \cdot s}{\mu m}$)	182	492

This molecular description assumed both a constant off-rate and linear force ex-

tension of cross-links. In the event that binding kinetics are regulated by the state of extension, we would expect (based on Rf) to find a region that exhibits a stick-slip behavior instead of the smooth. Depending on the nature of any coupling between cross-links local stick-slip could either give rise to a global stick-slip behavior or a heterogenous mixture of stuck and sliding cross-links. It would be interesting to explore this topic further in the future, but in the present analysis, we choose to ignore complications from these nonlinear effects.

CHAPTER 7

DISCUSSION AND FUTURE DIRECTIONS

APPENDIX A
WORKSHOP ON MODELING IN BIOLOGY

APPENDIX B
ARTISTIC INTERPRETATIONS OF FILAMENT
RECYCLING

APPENDIX C

REDUCING POWER CONSUMPTION IN HIGH PERFORMANCE COMPUTING

C.1 Introduction

Data centers in the US consume an estimated 91 billion kilowatt-hours yearly, equivalent to the annual output of 34 large coal-fired power plants.[?] These same estimates show that only 6-12% of the electricity is used for powering servers while the rest is used to keep machines idling, wasting resources and money in the process. Data center electricity is not inexpensive, costing American businesses \$13 billion annually in electricity bills.[?] Because cost is a strong motivating factor for businesses and universities, we consider data center energy efficiency in the context of cost savings for data center operations.

Demand response (DR) programs provide incentives to induce dynamic management of customers electricity load in response to power supply conditions, for example, reducing their power consumption in response to a request from the utility.[?] Anita can you add something around here that points out how demand response also increases the sustainability of the datacenter beyond just cost reduction. Many energy providers have Voluntary Load Response (VLR) programs, which encourage commercial consumers to reduce power demands during peak periods, such as particularly hot summer days. Participants are given between one and four hours notice of a request to shed some of their electric load, with two and eight hours of participation and the expectation to shed at least 10 kilowatts. We are interested in exploring more active ways in which to participate in electricity demand response programs while impacting the users minimally.

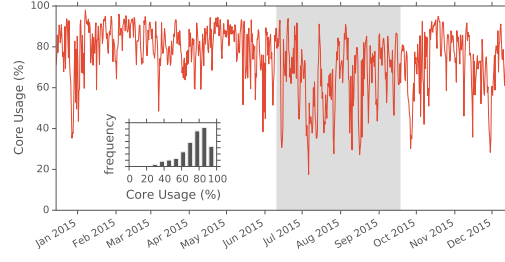


Figure C.1: Average core usage for a 244 node shared HPC partition in the Midway cluster. Insert shows usage statistics histogram.

In many university data centers, a significant portion of the data center is dedicated to high performance research computing which is typically Tier 1. While these jobs take longer periods of time to complete, they are less time sensitive and more flexible than systems which support core business functions such as the university's email. We wish to use the flexibility in scheduling of these jobs to reduce energy consumption of university data centers during periods of peak energy demand.

As shown in the example core usage data of Figure C.1, although the typical average usage during the school year is a fairly standard 80%, the averaged workload can fall to 65% of full capacity in the hottest summer months from June to September. These months also present the period of greatest electricity demand due largely to increased usage of air conditioning. This presents a valuable opportunity to potentially curtail electricity use in demand response scenarios by shifting load off of the peak periods of energy price. Toward this aim, this paper is our attempt to estimate the economic savings, feasibility, and any potential user impact from full or partial cluster shutdown during periods of increased energy demand.

C.1.1 Alternative Demand Response Options in Data Centers

Although we focus on load shifting for our study, we wish to point out prior work on alternative strategies for demand response.

Facility changes A study by Lawrence Berkeley National Laboratory (LBNL) found that 5% of the data center load can typically be shed in 5 minutes and 10% of the load can be shed in 15 minutes without changes to how the IT workload is handled, i.e., via temperature adjustment and other building management approaches[?]. Most data centers have local power due to a backup generator, which could also be used to absorb some load during peak time [?]. More recently, methods of energy storage have been proposed[?] in which UPS batteries are re-purposed for provisioning during periods of peak demand in addition to their primary purpose of backup power. However, these methods all entail manual intervention, with close monitoring and control.

Power capping is a strategy by which to run data center equipment within a set of constraints which assume the electricity draw for the data center as a whole cannot grow any larger. Some examples of this include and turning off or constraining CPU/GPU power consumption to values below the CPU Thermal Design Power (TDP) value, which requires less voltage. Many equipment manufacturers - including IBM, Intel and AMD - have implemented power capping technology that can be monitored at the processor level and applied at the rack level. One approach to power capping is Dynamic Voltage/Frequency Scaling (DVFS). However, as noted by Roundtree[?], no machine in the Top 500 list of supercomputers makes use of DVFS to save power or energy since the performance impact and the amount of power and energy saved was highly application dependent. Power capping doesn't necessarily equate to energy efficiency nor cost savings.

Schedulers Zhou et al[?] present a method for power-aware scheduling by using a combination of a scheduling window and 0-1 knapsack model, which shows promise. However, since SLURM is our scheduler, we decided to focus solely on SLURM. Bodas et al[?] demonstrate an integration of power capping into a power-aware scheduler, with the overall goal of maintaining average system power within a budget. Their work demonstrates that SLURM's auto mode can be used to maximize available power.

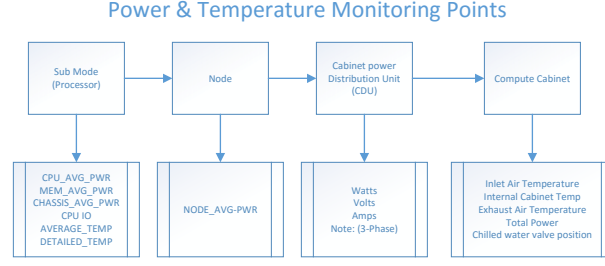


Figure C.2: Energy monitoring framework.

C.2 Problem Statement

Can load shifting of high performance computing tasks save universities money in energy demand response scenarios? To explore the relative costs of implementing load shifting in demand response scenarios, we have expressed the problem by modeling total dollar cost. We wish to use this framework to explore the optimization of price in the presence of various data center usage statistics and price fluctuation schemes.

C.2.1 Modeling Energy Costs

We generate a model total cost function composed of a fixed cost for purchasing and maintaining nodes plus a variable cost dependent on data center power usage and energy prices. We wish to minimize the cost function

$$C = p_n T n_{max} + \int_0^T dt \cdot p(t) \left(n(t)u(t) + u_w \frac{\Delta n(t)}{\Delta t} \right)$$

where $p(t)$ is the price of power at time t , $0 < n(t) < n_{max}$ is the number of running nodes, $u(t)$ is the average node power usage, u_w is the wasted power from turning on a node, p_n is the amortized lifetime cost of purchasing a node, and n_{max} is the total number of nodes in the cluster.

Based on our cluster usage statistics, we approximate that compute cycles are roughly interchangeable and that the main determiner of power usage is simply the CPU utilization of the node. In this case, node power usage takes the form

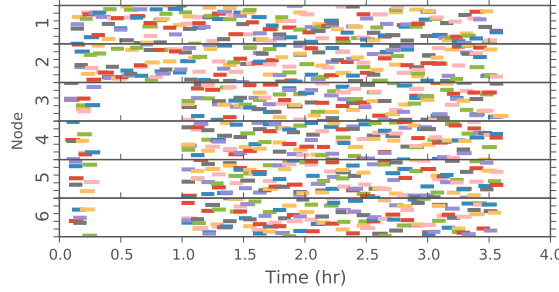


Figure C.3: Diagram of job scheduling during a four node temporary shutdown experiment. Each colored rectangle displays the execution time of a single LAMPPS test job running for approximately 5 minutes.

$$u(t) = u_0 + u_v \cdot r(t)$$

where $0 < r(t) < 1$ is the fraction of CPU usage, u_0 is the cost of an idling node and u_v is the variable cost for doing r work on a machine.

We wish to minimize the cost function C subject to the constraint that the sum of the submitted CPU cycles, S , are all completed after a period T .

$$\int_0^T dt \cdot n(t)r(t) = S$$

C.2.2 Response to a Temporary Price Spike

In particular, we wish to use this framework to determine how to run our data center in the situation where every T days, we see a "price spike" from p_0 to p_s , lasting time period t_s . This condition is highly similar to the one facility managers face when utility providers impose usage tariffs during peak energy demand periods.

In this situation, the number of running machines will change stepwise between a high number of running machines, $n_H = n_{max}$, and a low number of running machines, n_L , and a high and low CPU utilization $r_H = 1$, r_L , with a corresponding u_H and u_L as defined above. The high usage will occur during the cheap energy supply, and the low usage will occur during the price spike. Therefore we can rewrite our cost

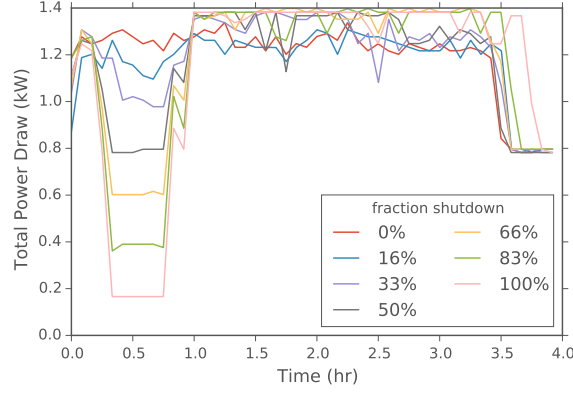


Figure C.4: Total power consumed during experiments where variable numbers of machines were shut down during simulated peak pricing.

function as

$$C = p_n n_H T + p_0 (u_0 + u_v) n_H (T - t_s) + p_s (u_0 + u_v r_L) n_L t_s + p_0 u_w (n_H - n_L) \quad (\text{C.1})$$

with the constraint

$$n_H (T - t_s) + n_L r_L t_s = S \quad (\text{C.2})$$

Inserting the constraint into our cost function to replace r_L yields

$$C = p_s u_v S + n_L \cdot (p_s u_0 t_s - p_0 u_w t_w) + n_H \cdot (p_n T + p_0 u_w t_w - (\Delta p u_v - p_0 u_0) (T - t_s)) \quad (\text{C.3})$$

where we've introduced the price difference, $\Delta p = p_s - p_0$.

We can analyze the change in costs as a function of n_L and n_H to determine the optimal cluster setup for known variables, t_s , p_s , p_n , p_0 , u_0 , u_v , and u_w .

From this analysis, whenever $p_s u_0 t_s < p_0 u_w t_w$, the cost of powering off nodes exceeds the cost of running those nodes idle so $n_L = n_H$ and $r_L = S/n_H t_s - (T - t_s)/t_s$. Otherwise powering off nodes saves money so the nodes that remain on run at full

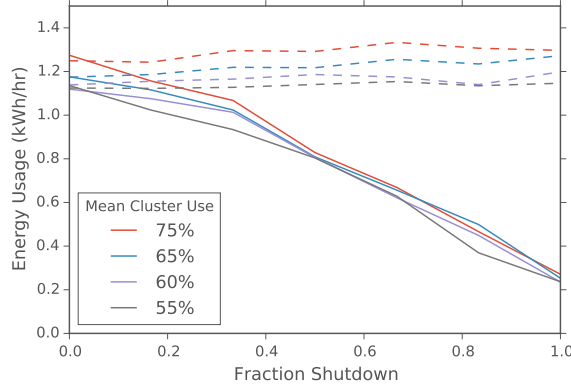


Figure C.5: Energy usage of test cluster during partial shutdown experiments. Solid lines indicate power usage during the shutdown, while dashed lines indicate power usage after returning to full operation.

capacity $r_L = 1$, and n_L is minimized subject to constraints giving $n_L = S/t_s - n_H(T - t_s)/t_s$.

If we can freely choose n_H to optimize cost, then whenever $(\Delta p u_v - p_0 u_0)(T - t_s) > p_n T + \min(p_0 u_w t_w, p_s u_0 t_s)$, we would increase n_H (i.e. buy more machines) until all the work is done during the cheap energy period. Therefore $n_H = S/(T - t_s)$ and either n_L or r_L is 0. Otherwise, the cost of new machines is more than any cost savings achieved from exploiting the price difference, and we would simply ignore the price spike (i.e. set $n_H = n_L = S/T$ and $r_L = 1$).

C.3 EDEALS: Electricity Demand-response Easy Adjusted Load Shifting

For a data center manager to use the above model to determine their cost savings, they must collect and analyze usage and power data on their system. We have built a cluster data processing pipeline, EDEALS, to assess the magnitude of potential savings available from a full or partial cluster shutdown. We combine SLURM job scheduling, node level IMM power and usage metrics, and cabinet level CDU measurements to determine the optimum magnitude of demand response cluster shutdowns.

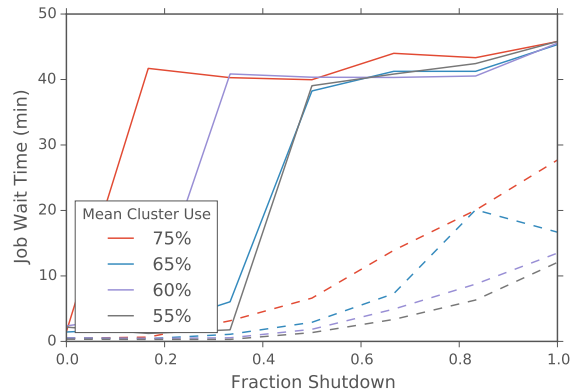


Figure C.6: Maximum (solid) and mean (dashed) job wait times during partial shut-down experiments.

Here we describe our data center instrumentation, so that we ensure accurate measurements of performance of the workload management system and HPC cluster alone without the influence of extraneous components. Since our focus is the HPC cluster and SLURM manager, we need to ensure those components alone affect the reduced data center utility bill. As depicted in Figure C.2, we take measurements at the core, node, rack, and cabinet level. These data are combined to detect power losses at each step and to determine the correlation between the power measurements at the machine level and the true power draw at the facility level.

Combining this data with electricity pricing statistics from utility managers allows system administrators to determine when and by how much to reduce their power usage to save money. We have built a set of scripts particular to our system to implement machine level power down in response to predicted energy peaks. At the end of the peak energy period the machines automatically reboot and are added by to SLURMs available server pool. At this time, these power cycling scripts are manually executed by system administrators after evaluation of the likelihood of near-term energy demand peaks. However, as more data centers begin to implement smart metering, it will become possible to automate load shifting in response to real-time energy pricing indicators. We look forward to continuing this as future work.

C.4 Small-Scale Evaluation of EDEALS

To test our load shifting scheme, we launched a series of small-scale experiments on a 6 machine test cluster using SLURM batch management system to schedule jobs. We wished to compare the energy savings and job wait times during a full or partial cluster shutdown in response to an energy price spike.

C.4.1 *Experimental Setup*

We measured the total energy use over a 3.5 hour window of which the first 30 minutes comprised a partial cluster shutdown, followed by a 15 minute powerup routine. We explored the impact of shutting down between one and all six nodes during the 30 minute window. The shutdown was carried out by fully powering nodes off. We compared this to the energy usage without the partial shutdown.

Identical sample jobs were submitted to the cluster via SLURM scheduler at a constant rate to set the average cluster usage to approximately 55%, 60%, 65% and 75% capacity. We used custom state control commands to set the power states of individual machines in the test cluster. The SLURM scheduler automatically shifted queued jobs to run on the available machines, as shown in the example job schedule displayed Figure ?? from a four node shutdown experiment. We used our EDEALS data analysis pipeline to measure the changes in energy usage and job wait time in the queue.

C.4.2 *Evaluation of Model Parameters*

Importantly, EDEALS allowed us to determine appropriate power parameters, u_0 , u_v , and u_w for both our test rack as well as a larger partition of the University of Chicago’s Midway production cluster. Figure C.7 shows the measured relationship between CPU utilization and energy usage as determined from the machine level IPMI metric data.

To account for losses not measured at the IPMI level, we compare the sum IPMI power usage to the rack level power monitoring. This comparison revealed a correction

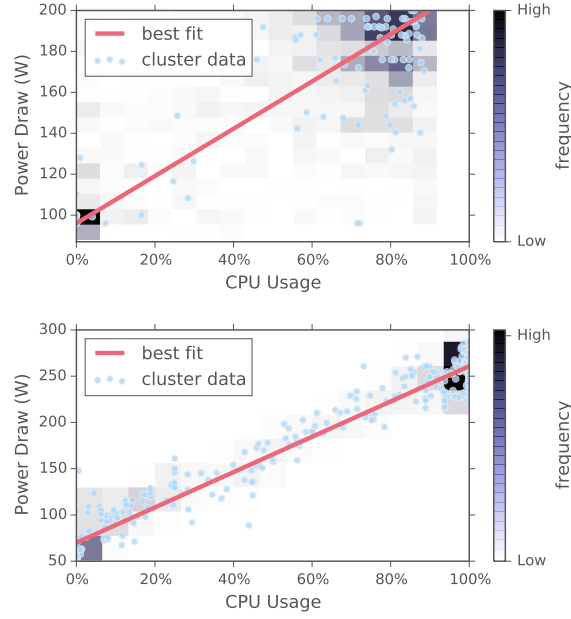


Figure C.7: Power data for test cluster (top) and production cluster (bottom) nodes in presence of variable usage. The slope and intercept of the line are used to determine u_v and u_0 respectively.

factor of 1.25 between the IPMI measurement and the total rack level energy draw. Using this corrected model, we were able to predict power consumption at the CDU level via CPU utilization under variable scheduler loads.

C.4.3 Relative Energy Savings and Max Wait Times

Our test cluster provided us with an important baseline in determining the effectiveness of a partial shutdown in reducing energy usage. As shown in Figure C.4, the total power draw from the test cluster was reduced dramatically during the shutdown period, and then returned to its baseline level.

These experiments were repeated with different job submission rates such that the average CPU usage varied from 55% to 75%. As shown in Figure C.5, the partial shutdowns reduced the total energy usage as measured at the CDU level. Not surprisingly, the power usage during cluster shutdown for all usage levels converged to roughly the same value at the point where all remaining operational machines reached

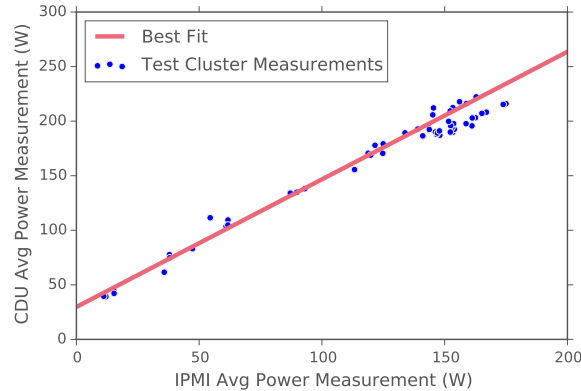


Figure C.8: Comparison between node level IPMI measurements and rack level CDU measurements. Best fit shows the model relationship used to convert IPMI data to estimated total power draw.

full capacity. Interestingly, the energy savings did not appear to be perfectly directly proportional to the fraction shut down. In particular, there was residual energy use associated with our machine’s low power state even when the cluster was entirely shut down.

We also measured the difference between job submission and start time, as depicted in Figure C.6. As one would expect, both mean and max wait times increased as the shutdown fraction grew and the effect was more pronounced when the cluster usage was higher. However, we were pleasantly surprised to find that max wait times topped out at 45 minutes, which was the duration of the entire cluster down period. This indicates that SLURM doesn’t add too much additional overhead, and therefore, the worst-case user wait times would not exceed the total period that the cluster was shut down.

C.5 Conclusion: Implication for An Operational HPC Datacenter

In an HPC datacenter, the variable cost to supply electricity to a facility can be decomposed into both a nominal cost per kilowatt-hour and a procurement cost from

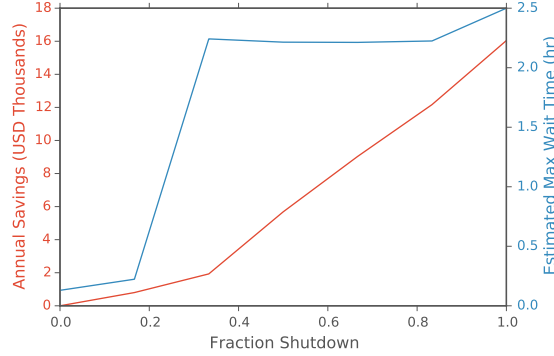


Figure C.9: Estimated savings from partial cluster shutdowns.

T	t_s	p_0	p_s
360 hr	2 hr	\$0.03/kWh	\$6.5/kWh

Table C.1: Model parameters estimated for medium scale HPC datacenter.

the supplier. Some suppliers impose a substantial procurement tariff based on electricity usage during the five, two hour long periods of highest demand in a year. In this scenario, the savings of load shedding can be orders of magnitude higher than the nominal price per kilowatt-hour. We estimate that by curtailing 1MW, 8 times per year, we can expect an annual savings of approximately \$100K, which in our case was roughly a 7

Combining these values with the power usage measurements from our production cluster, we can extrapolate the yearly savings based on fractional shutdowns of the data center. In addition, using the wait time statistics from our test cluster we can also estimate the worst-case impact on user wait-times that these cluster shutdowns will incur. We display this information in Figure C.9, as a function of the fraction of the cluster that we would be theoretically willing to shut down.

C.6 Acknowledgments

Special thanks goes out to Brandon for all his work getting our test cluster set up as well as for his useful input on machine pricing information. We also wish to thank

Matt Beach for his invaluable knowledge on energy pricing mechanisms and university power plans. Finally, we wish to thank Dr. Birali Runesha for his support in carrying out this project.

C.7 Availability

On our Github, we have provided all data collection scripts, analysis routines, and experimental setups, as well as detailed calculations and optimization methods for other price models.

`https://github.com/rcc-uchicago/datacenter`